

Stabilizing Lithium Metal Anode by Ion Depletion-Induced Phase Transformation in Polymer Electrolytes

Qian Cheng, yupeng miao, Zhe Liu, James Borovilas, Hanrui Zhang, Shuwei Liu, Haozhen Wang, Xi Chen, Long-Qing Chen, Wei Min, Yuan Yang

Submitted date: 06/02/2021 · Posted date: 08/02/2021

Licence: CC BY-NC-ND 4.0

Citation information: Cheng, Qian; miao, yupeng; Liu, Zhe; Borovilas, James; Zhang, Hanrui; Liu, Shuwei; et al. (2021): Stabilizing Lithium Metal Anode by Ion Depletion-Induced Phase Transformation in Polymer Electrolytes. ChemRxiv. Preprint. <https://doi.org/10.26434/chemrxiv.13726243.v1>

Ion depletion in liquid electrolytes is widely accepted to promote dendrite growth in metal anodes due to enhanced local electrical field and magnified concentration fluctuation at the electrode/electrolyte interface. Here we report unexpected opposite behaviors in solid polymer electrolytes, showing that ion depletion leads to uniform lithium deposition. Such stabilization originates from ion depletion-induced phase transformation, which forms a new PEO-rich but salt/plasticizer-poor phase at the lithium/electrolyte interface, as unveiled by stimulated Raman scattering microscopy. This new phase leads a significantly higher Young's modulus (~2-3 GPa) than the bulk polymer electrolyte (< 10 MPa), which effectively suppresses dendrite growth. Further battery tests show that $\text{LiFePO}_4/\text{PEO}/\text{Li}$ cells with such ion depletion-induced phase transformations can be reversibly cycled for 200 times, while cells without such transformation fail within only ten cycles, demonstrating the effectiveness of this strategy to stabilize the lithium anode.

File list (9)

Stabilizing Lithium Metal Anode by Ion Depletion-induced ... (2.50 MiB)	view on ChemRxiv • download file
Stabilizing Lithium Metal Anode by Ion Depletion-induced ... (1.49 MiB)	view on ChemRxiv • download file
SI for Stabilizing Lithium Metal Anode by Ion Depletion-ind... (3.52 MiB)	view on ChemRxiv • download file
Suppl Movie 6.mp4 (4.44 MiB)	view on ChemRxiv • download file
Suppl Movie 5.mp4 (10.76 MiB)	view on ChemRxiv • download file
Suppl Movie 4.mp4 (1.72 MiB)	view on ChemRxiv • download file
Suppl Movie 3.mp4 (2.51 MiB)	view on ChemRxiv • download file
Suppl Movie 2.mp4 (2.57 MiB)	view on ChemRxiv • download file

Suppl Movie 1.mp4 (1.09 MiB)

[view on ChemRxiv](#) • [download file](#)

Stabilizing Lithium Metal Anode by Ion Depletion-Induced Phase Transformation in Polymer Electrolytes

Qian Cheng,^{1,6} Yupeng Miao,^{2,6} Zhe Liu,³ James Borovilas,¹ Hanrui Zhang,¹ Shuwei Liu,¹ Haozhen Wang,⁴ Xi Chen,^{4,5} Long-Qing Chen,³ Wei Min,^{2*} Yuan Yang^{1*}

¹ Program of Materials Science and Engineering, Department of Applied Physics and Applied Mathematics, Columbia University, New York, NY 10027, USA

² Department of Chemistry, Columbia University, New York, NY, 10027, USA

³ Department of Materials Science and Engineering, The Pennsylvania State University, University Park, State College, PA 16802, USA.

⁴ Advanced Science Research Center (ASRC), City University of New York, 85 St. Nicholas Terrace, New York, NY, 10031 USA

⁵ Department of Chemical Engineering, The City College of New York, 160 Convent Avenue, New York, NY 10031, USA

⁶ These authors contributed equally

Correspondence: Y.Y. (yy2664@columbia.edu) or W.M. (wm2256@columbia.edu)

Abstract: Ion depletion in liquid electrolytes is widely accepted to promote dendrite growth in metal anodes due to enhanced local electrical field and magnified concentration fluctuation at the electrode/electrolyte interface. Here we report unexpected opposite behaviors in solid polymer electrolytes, showing that ion depletion leads to uniform lithium deposition. Such stabilization originates from ion depletion-induced phase transformation, which forms a new PEO-rich but salt/plasticizer-poor phase at the lithium/electrolyte interface, as unveiled by stimulated Raman scattering microscopy. This new phase leads a significantly higher Young's modulus (~2-3 GPa) than the bulk polymer electrolyte (< 10 MPa), which effectively suppresses dendrite growth. Further battery tests show that LiFePO₄/PEO/Li cells with such ion depletion-induced phase transformations can be reversibly cycled for 200 times, while cells without such transformation fail within only ten cycles, demonstrating the effectiveness of this strategy to stabilize the lithium anode.

Introduction

Lithium-metal batteries (LMBs) have attracted significant attention in recent years for next-generation energy storage with high energy density^{1, 2, 3}. Li metal anode has a theoretical capacity of 3860 mAh g⁻¹, ten times that of the conventional graphite anode, and an ultralow electrode potential (-3.04 V vs. standard hydrogen electrode / SHE). However, lithium deposition is prone to being non-uniform, leading to rough morphologies such as mossy and dendritic lithium^{4, 5, 6, 7}. Such uneven deposition not only results in a large electrode surface area which promotes side reactions with electrolyte and decreases coulombic efficiency and cycle life^{8, 9}, but also imposes potential safety hazards such as internal shorting and thermal runaway, especially in combination with conventional flammable liquid electrolytes (e.g. ethers and carbonates)^{10, 11, 12, 13}.

Polymer electrolytes are appealing for enhancing the thermal stability of LMBs as they are much more thermally stable than liquid electrolytes^{14, 15, 16}. For example, the flash points (f.p.) of poly (ethylene oxide) is 250 °C¹⁷, much higher than dimethyl carbonate (21.5 °C)¹⁸, 1,3-dioxolane (2 °C)¹⁹ and 1,2-dimethoxyethane (-2 °C)¹⁷ in liquid electrolytes. Polymer electrolytes are also compatible with conventional battery manufacturing processes and easy to scale up²⁰. Unfortunately, Young's moduli of PEO-based polymer electrolytes are typically in the range of 20 to 70 MPa^{21, 22, 23}, much lower than the proposed threshold of 1 GPa needed to suppress Li dendrites^{11, 24}. Hence, the fast growth of Li dendrites in polymer electrolytes is widely observed in literature^{24, 25, 26}, and Supplementary Movie 1. The dendrite growth becomes even more severe with the introduction of plasticizers for enhancing ionic conductivity, as they further soften the electrolyte^{23, 27}. This issue is difficult to be fully resolved by ceramic additives,²⁸ since lithium dendrites can still penetrate through the interspace between ceramic fillers. Currently, Li dendrite growth remains one of the major challenges in polymer electrolyte-based LMBs.²⁹

Addressing this issue requires fundamental understanding of the embedded dynamic Li metal/polymer electrolyte interface, such as how Li⁺ heterogeneity evolves at the Li anode surface and how the Li anode interacts with solid electrolytes. While remarkable advances have been achieved recently in characterizing the Li anode and solid electrolyte interphase (SEI) in liquid electrolytes, such as cryo-transmission electron microscope (TEM),^{30, 31, 32} nuclear magnetic resonance (NMR),^{33, 34} *in-situ* and environmental TEM,^{35, 36} synchrotron,^{37, 38} and

ambient pressure XPS³⁹, there is limited progress towards imaging the interaction between Li⁺ transport in the electrolyte and Li dendrite growth. This arises from challenges in visualizing ions in the electrolyte, which not only has a low concentration (0.01-2 M), but also possesses fast dynamics (diffusivity of $\sim 10^{-7}$ - 10^{-6} cm² s⁻¹) compared to solid electrodes (10-50 M, and $< 10^{-9}$ cm² s⁻¹). Hence, ultra-high chemical sensitivity (~ 1 -10 mM), high speed (~ 1 s/image), and fine spatial resolution (< 1 μ m) are simultaneously required to image the electrolyte, especially during ion depletion. Such resolutions and sensitivity are beyond the capability of conventional characterization tools.

Recently we utilized stimulated Raman scattering (SRS) microscopy to image ion transport profile in liquid electrolytes, which simultaneously offers high sensitivity (< 1 mM), fast imaging speed (~ 2 μ s per pixel), and fine spatial resolution (down to 300 nm)^{40, 41, 42}. SRS microscopy uses two temporally and spatially synchronized laser beams with an energy difference equal to that of the target bond's vibrational mode. The synergy of the two beams amplifies the otherwise weak vibrational signal by up to 10^8 times. It thus enables the desired resolutions, imaging speed, and sensitivity (**Fig. 1a**, Supplementary Fig. 1).⁴³ Using this emerging microscopy, we visualized for the first time the heterogeneity of ion depletion in liquid electrolytes and how it correlated with lithium dendrite growth.⁴⁰ We observed that ion depletion at the Li/electrolyte interface led to faster dendrite growth due to the enhanced electrical field and larger concentration heterogeneity, which agreed with theoretical predictions.^{1, 44}

In this report, we further explored the solid polymer electrolyte/electrode interaction and observed unexpected opposite phenomena. Instead of promoting dendrite formation, ion depletion strongly suppressed dendrite growth in PEO electrolytes and led to reversible lithium plating and stripping. Further analysis unveiled that this unusual behavior originated from an ion depletion-induced phase transformation in the polymer electrolyte and subsequent mechano-chemical coupling inside (**Fig. 1b**). Once ions deplete, a new PEO-rich phase was formed at the lithium/electrolyte interface with a high modulus ~ 1 -3 GPa, as measured by atomic force microscopy (AFM). Such a high modulus suppressed dendrite growth and led to uniform lithium deposition. Based on this discovery, we developed a PEO electrolyte with an optimal composition (EO/Li = 6, ~ 1.6 M Li salt), which showed stable cycling over 200 times in an LFP/PEO/Li cell at 38 °C. In contrast, LFP/PEO/Li cells with concentrated electrolyte (EO/Li = 3,

~2.7 M Li salt) failed quickly after 10 cycles due to the rapid growth of lithium dendrites and dramatically increased impedance. This work proposes a new strategy for using self-forming mechanically strong phases to stabilize the lithium metal anode in solid-polymer-electrolyte-based LMBs.

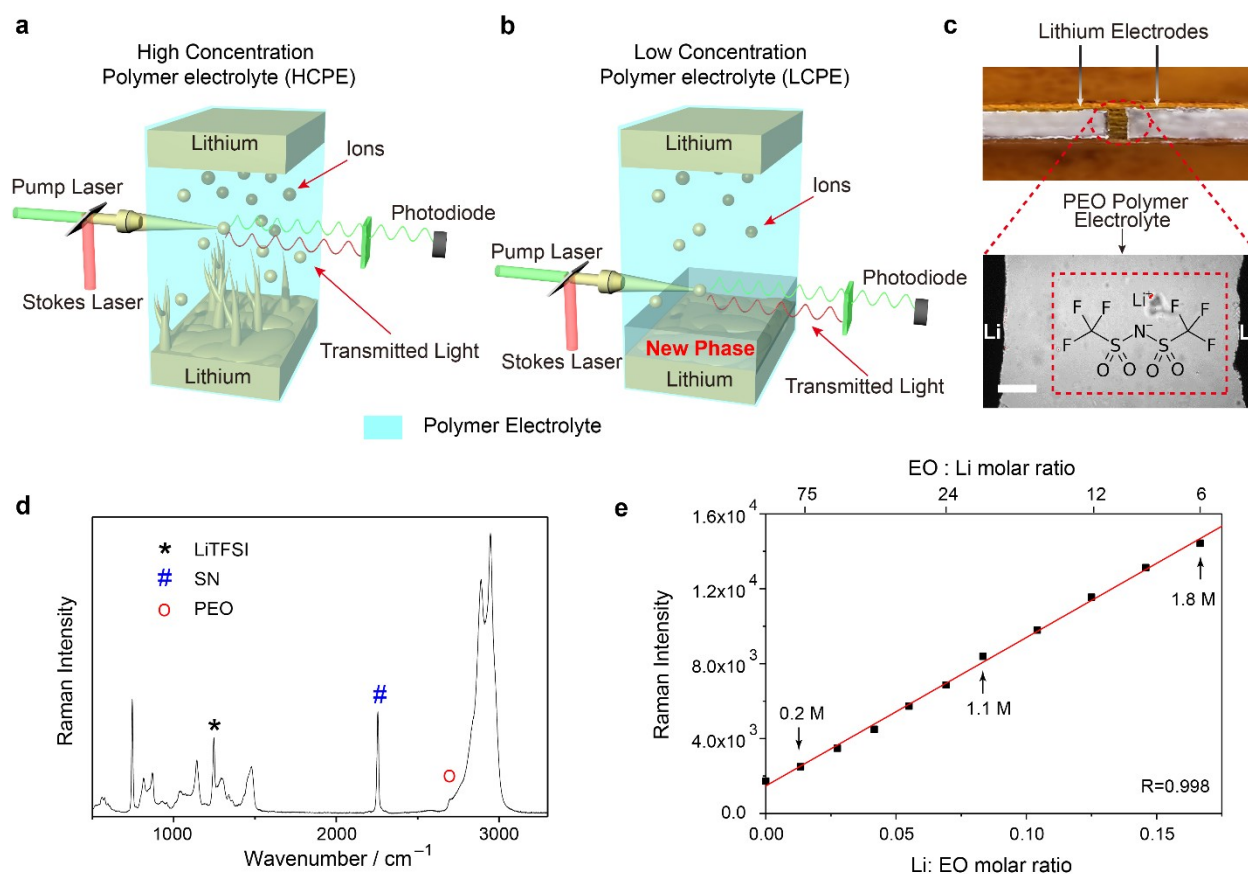


Figure 1. The schematics of *operando* SRS imaging of the Li/PEO electrolyte interface. The schematics of SRS observations on **a**, high concentration polymer electrolyte (HCPE) and **b**, low concentration polymer electrolyte (LCPE) in Li/Li cells. In LCPE, the ion depletion-induced phase transformation leads to a mechanically strong PEO-rich phase at the lithium/electrolyte interface, which helps suppress lithium dendrites. **c**, the bright field of a Li/PEO/Li cell *in operando*. The upper picture shows the structure of the cell, while the lower one shows a zoom-in image under the microscope. **d**, the Raman spectrum of LCPE, where signature peaks for LiTFSI, SN, and PEO are labeled. The corresponding composition of LCPE is EO: Li: SN = 12: 1: 2.64. **e**, the plot of Raman intensity of the LiTFSI peak at 1245 cm^{-1} versus the Li: EO ratio in PEO electrolytes with 40 wt% SN, showing good linearity. The points of 1.1 M and 1.8 M LiTFSI correspond to LCPE and HCPE, respectively.

Results

SRS imaging of Li / solid polymer electrolyte interaction. Home-made parallel cells were used to visualize the Li / PEO electrolyte interaction via SRS microscopy (**Fig. 1c**). In this cell, the PEO electrolyte filled in the gap between two pieces of lithium, and all components were sandwiched between two glass slides and sealed by epoxy. The distance between two electrodes was typically ~ 0.5 mm. The PEO electrolyte contained lithium bis(trifluoromethanesulfonyl) imide (LiTFSI) as the salt and succinonitrile (SN) as the plasticizer⁴⁵ to enhance ionic conductivity and enable operation at room temperature. Wavenumbers at 1245 cm^{-1} (CF_3 stretching),⁴⁶ 2250 cm^{-1} ($\text{C}\equiv\text{N}$ stretching),⁴⁷ and 2800 cm^{-1} (C-H stretching with combination vibration)⁴⁸ were selected for SRS imaging of LiTFSI, SN and PEO, respectively (**Fig. 1d**). Due to the requirement of electroneutrality, $[\text{Li}^+]$ could be considered to be equal to $[\text{TFSI}^-]$, even at the nanoscale (Supplementary Note 2), with an error smaller than 0.1 mM .⁴⁰ Therefore, $[\text{TFSI}^-]$ was measured to represent the local $[\text{Li}^+]$. The Raman intensity of TFSI^- is proportional to its concentration. Hence the Raman signal can be easily converted to chemical concentrations (**Fig. 1e**). The chemical sensitivity of LiTFSI was calculated to be 0.012 M .

Lithium growth in PEO electrolytes with high and low concentration. As two representatives, the high-concentration polymer electrolyte (HCPE) and the low-concentration polymer electrolyte (LCPE) were studied with EO: Li: SN = 12: 2: 2.64 and 12: 1: 2.64 in molarity, respectively, which corresponded to 1.8 M LiTFSI and 2.4 M SN for HCPE, and 1.1 M LiTFSI and 2.9 M SN for LCPE. The weight ratios of SN to PEO were fixed at 40% in both cases. Their ionic conductivities are $1.7 \times 10^{-4}\text{ S cm}^{-1}$ (HCPE) and $1.0 \times 10^{-4}\text{ S cm}^{-1}$ (LCPE) at room temperature (RT), respectively (Supplementary Fig. 2). Due to the relatively low ionic conductivities at RT, a current density of 0.5 mA cm^{-2} was applied.

In the case of HCPE (**Fig. 2a & Supplementary Movie 2**), the applied current gradually depleted $[\text{Li}^+]$ on the lithium surface ($[\text{Li}^+]_{0\text{ }\mu\text{m}}$) from 1.8 M at $t = 0$ to 1.2 M at $t = 27\text{ min}$, after which $[\text{Li}^+]_{0\text{ }\mu\text{m}}$ remained at $\sim 1.2\text{ M}$ in a steady state (**Fig. 2b & c**). Meanwhile, the lithium growth rate (\mathbf{v}) quickly increased from $0.27 \pm 0.18\text{ }\mu\text{m min}^{-1}$ at $t = 0$ to $0.9 \pm 0.46\text{ }\mu\text{m min}^{-1}$ at $t = 27\text{ min}$ (**Fig. 2d**). The growth was in the form of mossy lithium, and statistical analysis showed a normal distribution of \mathbf{v} (Supplementary Fig. 3a-c). Afterwards, \mathbf{v} was drastically increased to

$\sim 1.5 \mu\text{m min}^{-1}$ for the remaining time, leading to an ultrahigh porosity of 97%, indicating that the HCPE could not suppress dendrite growth at all. A dual-peak normal distribution was observed at this stage (Supplementary Fig. 3d-h), where v was low in part of the surface ($< 1 \mu\text{m min}^{-1}$), but ultrahigh in other regions ($> 2 \mu\text{m min}^{-1}$), showing the heterogeneous dendrite growth on lithium electrode. This dual-peak mode may arise from SEI properties and non-uniform depletion of ions. These results shows that if no phase transformation occurs, ion depletion at the Li/polymer electrolyte interface promotes dendrite growth (Supplementary Movie 2), similar to our previous observations in gel electrolyte.⁴⁰

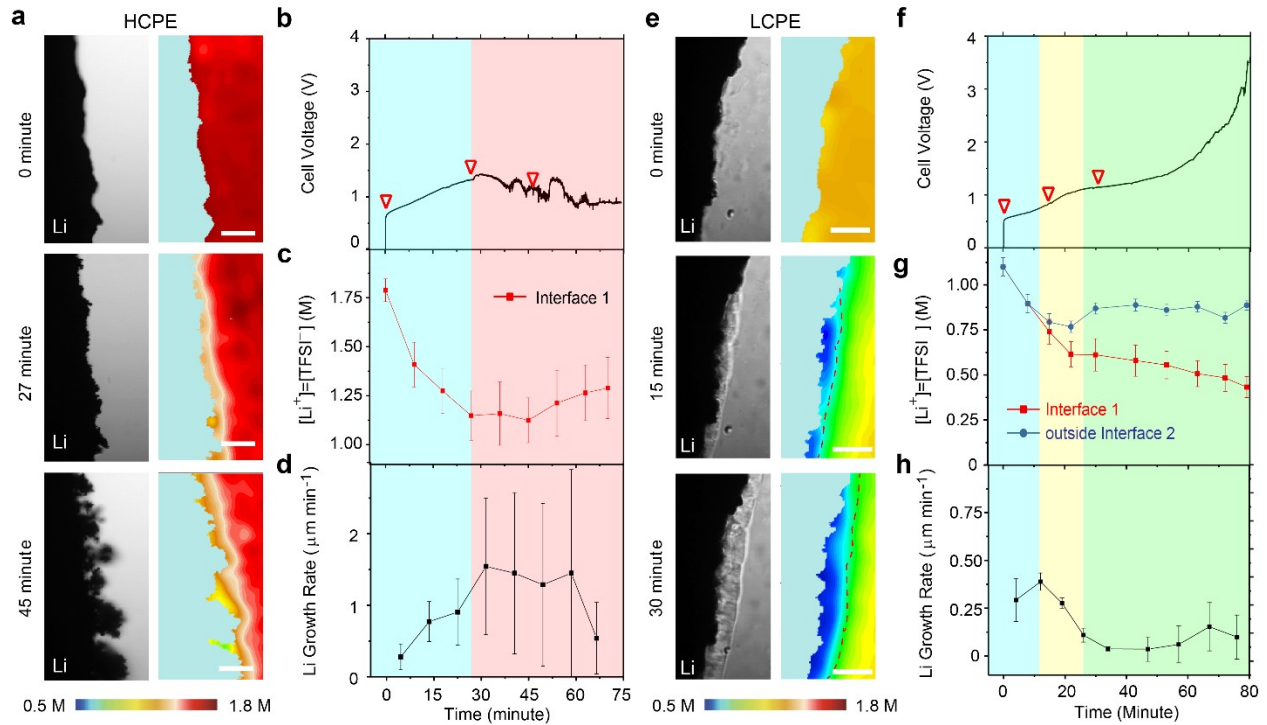


Fig. 2. Lithium growth at the lithium/PEO electrolyte interface with HCPE or LCPE. **a-d**, lithium dendrite growth in HCPE. **a**, the bright field and corresponding SRS images of $[\text{Li}^+] = [\text{TFSI}^-]$ at three representative stages. **b**, the voltage profile of the Li/Li cell. **c**, $[\text{Li}^+] = [\text{TFSI}^-]$ versus time, and **d**, the lithium growth rate (v) versus time. Interface 1 refers to the boundary between the lithium electrode and the PEO electrolyte. **e-h**, lithium growth in LCPE. **e**, the bright field and SRS images of $[\text{Li}^+]$ at three representative moments. **f**, the voltage profile of the Li/Li cell. The yellow shading corresponds to the appearance of the PEO-rich phase and the green shading indicates the regime where the PEO-rich phase has covered the entire lithium surface. **g**, $[\text{Li}^+] = [\text{TFSI}^-]$ versus time, and **h**, the lithium growth rate (v) versus time. Interface 2 refers to the boundary between the new PEO-rich phase and the isotropic bulk

polymer electrolyte, as marked by dash lines in SRS images in **e**. Scale bars are 50 μm . Zoom-in SRS images of **a** & **e** are shown in Supplementary Fig. 4.

In contrast to the conventional behaviors observed in HCPE, we find that ion depletion in LCPE induced a phase transformation process at the lithium/electrolyte interface that unexpectedly suppressed lithium dendrite growth, as observed by both SRS and bright-field (BF) images (**Fig. 2e** & Supplementary Movie 2). First, the new phase appeared as the blue color region in SRS and granular-like region in BF, which was confirmed by the spontaneous Raman spectrum (Supplementary Fig. 5). This new phase had a much lower [LiTFSI] than that in the isotropic bulk LCPE, as shown by the contrast between [LiTFSI] at the Li/electrolyte interface (interface 1), and [LiTFSI] outside the boundary between the new phase and the isotropic bulk electrolyte (interface 2). This difference increased from 0.79 M vs. 0.74 M at $t = 15$ min, to 0.87 M vs. 0.61 M at $t = 30$ min, and 0.89 M vs. 0.43 M at $t = 79$ min (**Fig. 2g**). Further study showed that the new phase was also poor in SN, [SN] was only ~ 1.8 M at the interface, compared to 3.8 M outside the interface 2 (Supplementary Fig. 6 and 7).

The appearance of this new phase unexpectedly but effectively suppressed the growth of lithium dendrites. Although the lithium dendrite growth was observed at $t = 0$ with v of $\sim 0.3 \mu\text{m min}^{-1}$ (87% porosity), v quickly dropped to $0.048 \mu\text{m/min}$ at $t = 30$ min after the initial formation of PEO-rich phase (**Fig. 2h**), equivalent to a porosity of 16%. At this stage, the PEO-rich phase progressively formed on the lithium metal surface. After the new phase fully covered the Li metal surface, the average v from 30 min to 63 min was only $0.044 \mu\text{m min}^{-1}$, which corresponded to a low porosity of 9.2%, about one thirtieth of that in HCPE, indicating a dense and uniform lithium deposition. Such behavior is not only self-forming but also self-reinforcing during ion depletion. For example, if Li dendrite grows fast at a certain location, the local current density will increase and lead to faster ion depletion and hence thicker new PEO-rich phase, which in turn suppresses dendrite growth (Supplementary Movie 1, LCPE). This active protection mechanism is distinct from other conventional passive protective layers, which requires perfect uniformity and durability. This suppression mechanism has not been reported in the literature, to the best of the authors' knowledge. This dynamic phase transformation and dendrite suppression are illustrated in Supplementary Movie 2.

The suppression mechanism and underlying mechano-chemical coupling. To understand how the new PEO-rich phase formed and suppressed dendrite growth, we first constructed the ternary phase diagram of PEO-LiTFSI-SN with the assistance of SRS (**Fig. 3a**), as it could measure the composition of each phase in a high-throughput fashion. The phase diagram illustrates a single-phase isotropic zone (I-zone) in the middle (orange), and three two-phase regions at the corners (white & contour region). Representative SRS images of each region are shown in Supplementary Fig. 8. As shown in **Fig. 3a**, the composition of HCPE is at the center of the I-zone. When a low-to-mid-level current is applied, it progressively reduces [LiTFSI] on the lithium metal surface (Path A in **Fig. 3a**). Due to the high salt concentration in HCPE, the electrolyte composition at the Li/electrolyte interface remains within the I-zone during ion depletion, and thus no phase transformation occurred. In contrast, the composition of LCPE is close to the boundary between the single-phase I-zone and the two-phase region, making it susceptible to undergoing a phase transformation in response to ion depletion (Path B in **Fig. 3a**), since forming two phases is thermodynamically more stable than staying in one phase. This phase transformation reduces not only [LiTFSI], but also [SN] in the new phase, as confirmed by the redistribution of [SN] during the phase transformation (Supplementary Movie 3 and Supplementary Fig. 6 & 7).

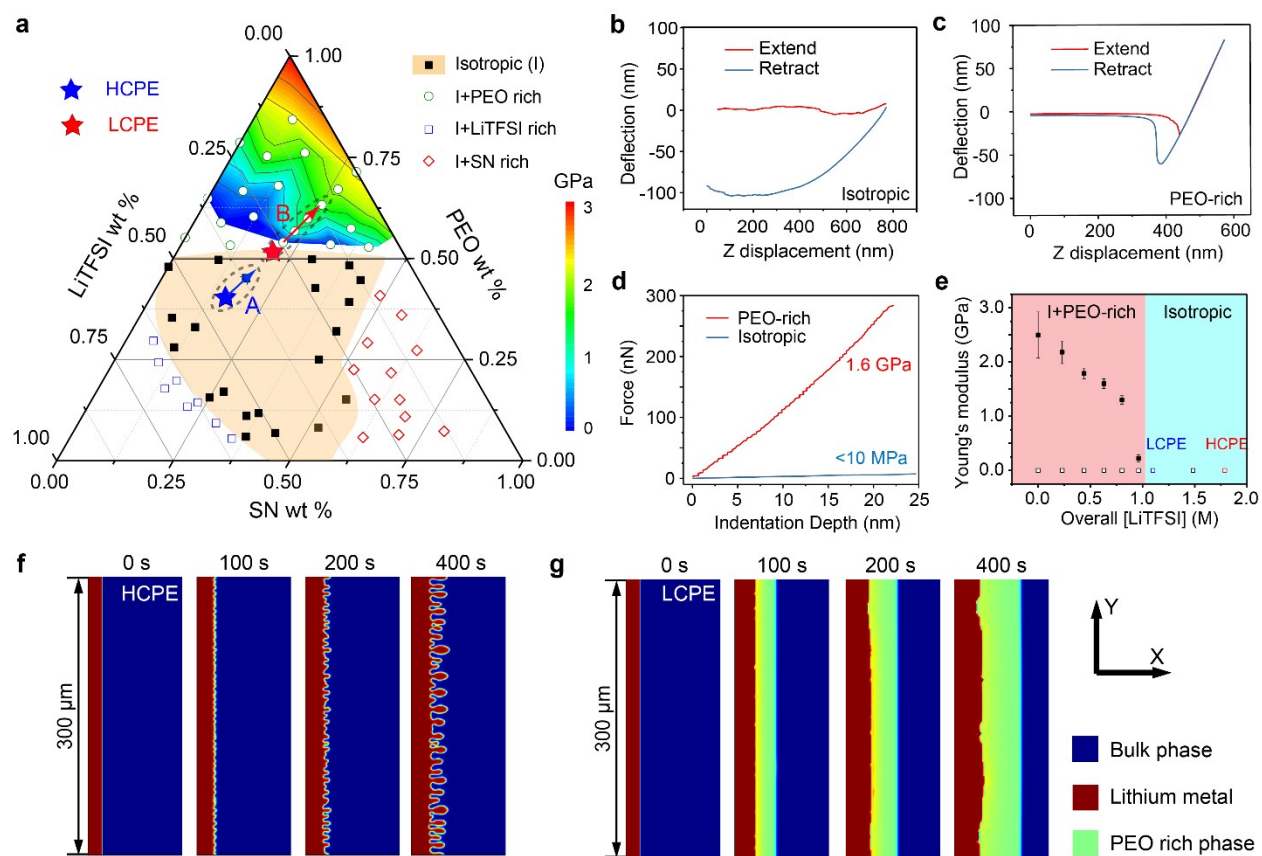


Fig. 3. The phase diagram and the mechanical properties of PEO-LiTFSI-SN polymer electrolytes.

a, the ternary PEO-LiTFSI-SN phase diagram in weight percentage. The orange color marks the region of the isotropic single-phase region, while other regions represent two phases. The rainbow color at the top of the triangle is the contour of Young's moduli of as-formed PEO-rich phases at corresponding compositions in the phase diagram. **b** & **c**, the AFM extending and retraction force curves of **b**, the isotropic bulk phase (I-zone, HCPE). No cantilever deformation is detected. **c**, the as-formed PEO-rich phase with a composition of 0.52 M LiTFSI and 2.6 M SN (See supplementary Table 1 for details). **d**, the corresponding force-indentation curves for samples in **b** and **c**. **e**, Young's moduli of the PEO-rich phase with different salt concentrations. The sample compositions are along the path A / B in **a**. All samples have the same SN/PEO ratio as HCPE and LCPE (40 wt%), but different [LiTFSI]. The exact composition of each phase is listed in Supplementary Table 1. The solid and empty squares show Young's moduli of the PEO-rich phase and the isotropic bulk phases, respectively. **f-g**, phase-field simulations of Li electrodeposition in solid polymer electrolytes with **f**, high concentration (2 M salt) and **g**, low concentration (1 M salt) at 0.5 mA cm^{-2} .

The effective suppression of Li dendrites by the new PEO-rich phase is hypothesized to arise from mechano-chemical coupling during the phase transformation at the Li/electrolyte interface. To verify this, AFM was used to measure the Young's moduli of solid polymer electrolytes (SPE) with different compositions, including both the I-zone and the PEO-rich phase, and the results are superimposed onto the phase diagram in **Fig. 3a**. For the composition of the HCPE (1.8 M LiTFSI and 2.4 M SN), the approaching curve showed no deformation of the cantilever when the tip was pressed into the electrolyte, indicating that the electrolyte was very soft (**Fig. 3b**). Large cantilever deflection is detected during tip retraction, confirming that the tip was pressed inside HCPE and the electrolyte was sticky. All SPEs within the I-zone and the isotropic phase of SPEs in the two-phase regions in **Fig. 3a** displayed similar results (Young's modulus $E < 10$ MPa), indicating they could not mechanically suppress lithium dendrite growth. Conversely, a classic force curve was observed for the PEO-rich phase formed in SPE. The sample had an overall composition of 0.6 M LiTFSI and 3.3 M SN, and the PEO-rich phase inside contained 0.52 M LiTFSI and 2.6 M SN (**Fig. 3c**). Using the Sneddon model,⁴⁹ the corresponding E was 1.6 GPa, well beyond the threshold to suppress lithium dendrites in previous studies,²⁴ thus explaining why dendrite growth was suppressed in LCPE. The conductivity of the as-formed PEO-rich state is in the order of 10^{-5} S cm^{-1} , which still allows Li^+ to shuttle (Supplementary Fig. 9).

To further understand mechano-chemical coupling at the Li/electrolyte interface, the composition-dependent mechanical properties of the PEO-rich phases in PEO electrolytes were systematically measured by AFM. As shown in **Fig. 3e**, the modulus of the PEO-rich phase quickly rises to 1.2 and 1.8 GPa when [LiTFSI] is reduced to 0.80 and 0.44 M in the PEO-rich phase (see Supplementary Table 1 for exact compositions in PEO rich phase). Further contour on the Young's moduli of the PEO-rich phases in the I + PEO-rich two-phase region (**Fig. 3a**) shows that the modulus is typically above 1 GPa when [LiTFSI] is less than 0.8 M. The contour indicates that the mechanism of ion depletion-induced stabilization of lithium deposition is effective in a wide range of electrolyte compositions.

The proposed suppression mechanism is also supported by phase-field simulations which take the mechano-chemical coupling into account (Supplementary Note 3 and Supplementary Movie 4). Since no new phase was formed in HCPE, lithium dendrites grew fast in the soft

isotropic bulk polymer electrolyte ($E = 10$ MPa, **Fig. 3f** & Supplementary Fig. 10a). In contrast, the rigid PEO-rich phase was formed ($E = 1.6$ GPa) once $[\text{Li}^+]$ was depleted below 0.85 M, effectively suppressing lithium dendrite growth (**Fig. 3g** & Supplementary Fig. 10b). The deposited lithium was largely uniform and the $[\text{Li}^+]$ heterogeneity was low on the lithium surface. These simulation results strongly agree with experimental observations, supporting the hypothesis that the formation of the PEO-rich phase with high Young's modulus suppresses dendrite growth.

Ion depletion-induced stabilization of Li anode in Li/Li and LFP/PEO/Li cells. With the understanding that the formation of a mechanically rigid PEO-rich phase can stabilize lithium deposition, we further examined the effectiveness of this strategy in repeated cycles. First, as a proof-of-concept experiment, 0.5 mA cm^{-2} was applied to a Li/PEO-LCPE/Li symmetric cell with a deposition capacity of 0.25 mAh cm^{-2} for 20 cycles at room temperature. As observed with the optical microscope (**Fig. 4a** & Supplementary Movie 5), no obvious lithium dendrites formed in the first deposition, and the lithium protrusions were frozen by the growing PEO-rich phase, leading to stable lithium deposition. During the lithium stripping, both the PEO-rich phase and lithium metal electrode shrank without forming any dead lithium. Upon cycling, the lithium surface moved forward slightly after 20 cycles, indicating that this suppression mechanism was effective upon multiple cycles. Further tests showed that such a reversible behavior could be achieved in a wide range of currents from 0.25 to 1 mA cm^{-2} (Supplementary Video 5). It should be noted that the PEO-rich phase sometimes did not fully disappear during lithium stripping, which is attributed to its disappearance being a kinetically slow process. In contrast, without the PEO-rich phase, fast dendrite growth was observed within the first several cycles for Li/Li cells with HCPE, forming large amounts of dead lithium during the repeated stripping process (**Fig. 4b** & Supplementary Movie 5).

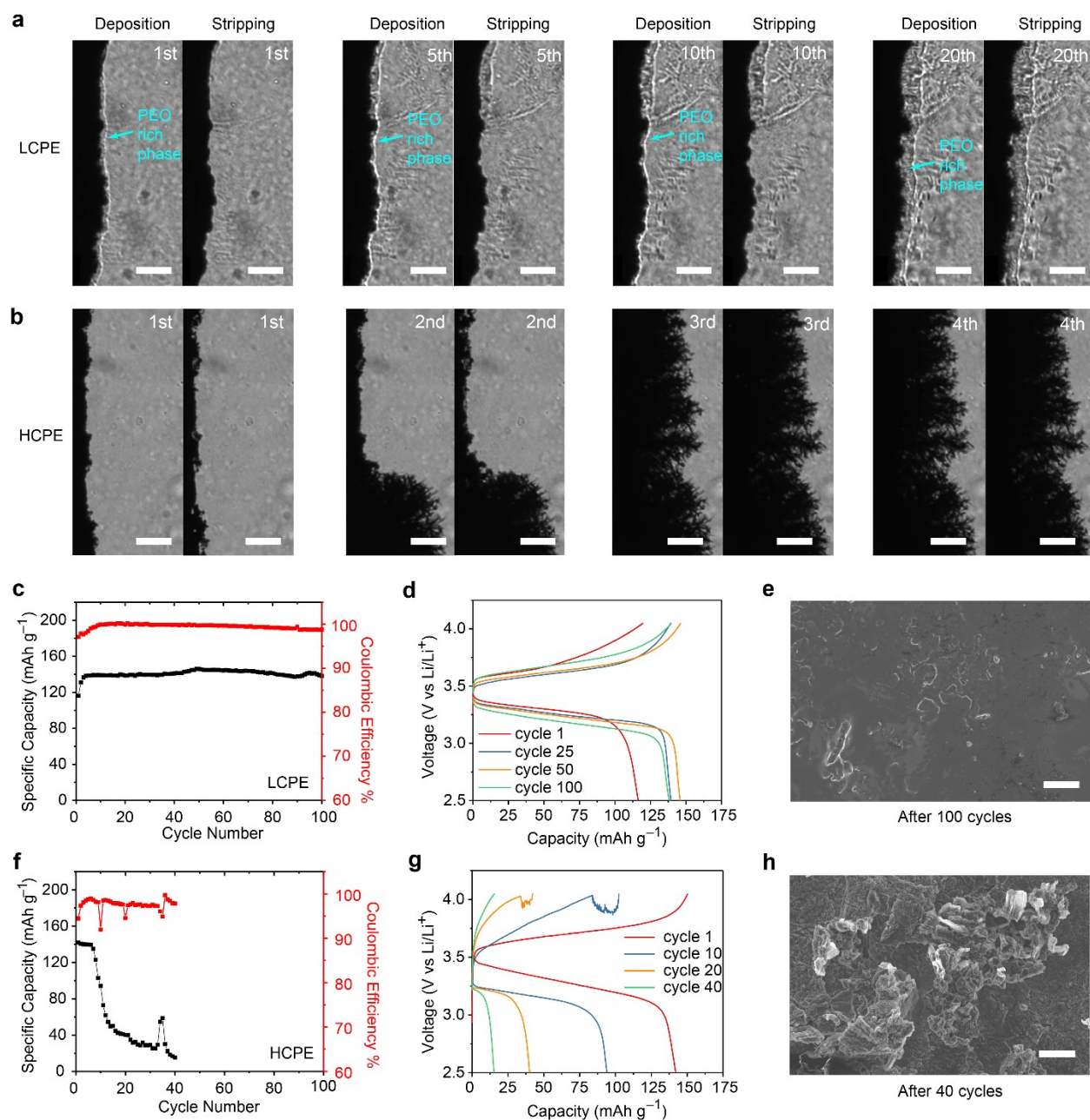


Fig 4. Cycling stability of the lithium metal anode in LCPE and HCPE. **a-b**, the bright-field images of the lithium electrodes during lithium plating and stripping in **a**. LCPE and **b**. HCPE. The scale bars are 100 μm . **c**, the cycling performance of $\text{LiFePO}_4/\text{Li}$ metal battery with LCPE and **d**, the corresponding voltage profiles. **e**, An SEM image of the lithium metal surface after 100 cycles. **f**, the cycling of $\text{LiFePO}_4/\text{Li}$ metal battery with HCPE and **g**, the corresponding voltage profiles. **h**, An SEM image of the lithium metal surface after 40 cycles. The scale bars in **e** and **h** are 10 μm .

The effectiveness of this strategy was further demonstrated in LFP ($\sim 4 \text{ mg cm}^{-2}$)/PEO/Li cells at 0.25 C and 40 °C. The PEO electrolyte was 100 μm -thick without a separator (Supplementary Fig. 11). Stable cycling was achieved with LCPE. The initial discharge capacity was 120 mAh g^{-1} and slowly increased to 141 mAh g^{-1} in the 4th cycle due to activation. After 100 cycles, the capacity remained at 140 mAh g^{-1} , corresponding to a retention of 99%. The average CE for cycle 5-100 is 99.6% (Fig. 4c). The voltage profile shows that the internal resistance only increases slightly and there is no sign of dendrite-induced short-circuit (Fig. 4d). SEM further revealed that the lithium metal surface was relatively flat after 100 cycles, with occasionally island-like morphology, demonstrating the effectiveness of the PEO-rich phase in suppressing lithium dendrites (Fig. 4e). On the other hand, the LFP/Li cell with HCPE quickly failed with the capacity dropping from 143 to 50.7 mAh g^{-1} after only 14 cycles (Fig. 4f). The voltage profile showed drastically increased overpotential, and the unstable voltage curve in charging suggests possible dendrite growth and micro-shorting (Fig. 4g). The average CE is only 97.4%, which probably arises from the prosperous growth of lithium dendrites, as validated by SEM imaging (Fig. 4h).

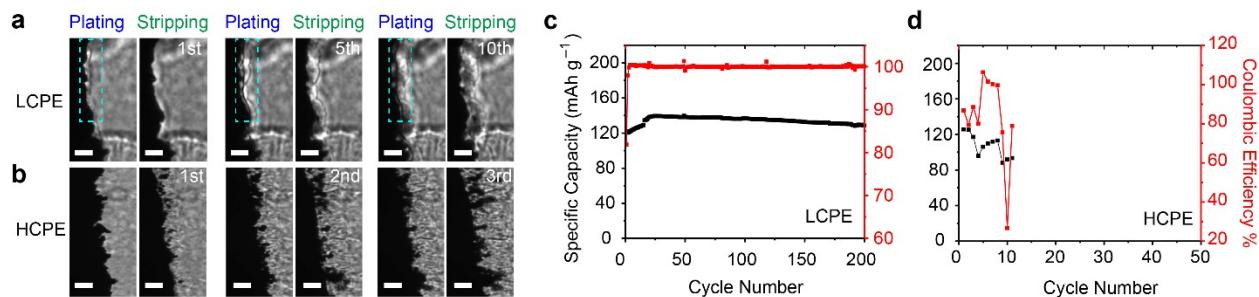


Fig 5. Cycling stability of the lithium metal anode in Li/Li cells and LFP/Li cells with PC/LiDFOB-LiBF₄ dual salt-based LCPE and HCPE. **a/b**, the bright-field images of the lithium electrodes in Li/Li cells with (a) LCPE and (b) HCPE at room temperature and 0.75 mA cm^{-2} . The scale bars are only $25 \mu\text{m}$ to better show the as-formed new PEO-rich phase (The dashed cyanic area). **c/d**, the cycling performance of LiFePO₄/Li metal batteries with (c) LCPE ($\text{EO/Li}^+ = 6$) and (d) HCPE ($\text{EO/Li}^+ = 3$) at 38 °C. The current density is 0.3 mA/cm^2 . In both LCPE and HCPE, PC is used as the plasticizer and it is 90 wt % of PEO.

Such phase separation-induced dendrite suppression is universal in PEO electrolytes. In another PEO electrolyte of lithium difluoro(oxalato)borate (LiDFOB) and lithium tetrafluoroborate (LiBF₄) as salts and PC as plasticizer, a similar phenomenon was also observed.

In this system, phase separation exists when $EO/Li^+ > 6$ and it diminishes at $EO/Li = 5.3$ (Supplementary Fig. 12), therefore, a PC-based LCPE with $EO/Li^+ = 6$ (2.9 mS cm^{-1}) was tested in a Li/Li cell at 0.75 mA cm^{-2} . A PEO-rich layer was clearly observed during lithium deposition and capable of suppressing lithium dendrites (**Fig. 5a** and Supplementary Movie 6). In contrast, phase separation was not observed in the PC-based HCPE with $EO/Li^+ = 3$ (5.2 mS cm^{-1}), and obvious dendrites and dead lithium were formed (**Fig. 5b**). The effectiveness of the strategy was also demonstrated in full cells. In an LFP/PC-based LCPE/Li cell with 5 mg LFP cm^{-2} and $40 \mu\text{m}$ thin lithium (**Fig. 5c**), the cell shows steady cycling over 200 cycles at 0.3 mA cm^{-2} (122 , 140 and 129 mAh g^{-1} in cycle 1, 25 and 200, respectively). In contrast, when LCPE was replaced by HCPE, the cell dies after ten cycles due to dendrite-induced internal shorting (**Fig. 5d**). The corresponding voltage profiles are shown in Supplementary Fig. 13. Batteries with $10 \text{ mg LFP cm}^{-2}$ (1.3 mAh cm^{-2}) and $40 \mu\text{m}$ lithium also showed stable cycling. The cell capacity is 116 mAh g^{-1} in cycle 1, 131 mAh g^{-1} in cycle 20 and 119 mAh g^{-1} in cycle 80 (Supplementary Fig. 14). Details of electrolyte composition and fabrication process can be found in Supplementary Note 1.

Conclusion

The dynamic ion depletion, phase transformation in polymer electrolytes, and their correlations with lithium deposition were observed for the first time thanks to the high chemical, temporal, and spatial resolutions of SRS microscopy. We successfully unveil phase transformation in the polymer electrolytes induced by ion depletion and the formation of a new PEO-rich phase at the electrode/electrolyte interface. This new phase has a high Young's modulus of up to 3 GPa , which is effective in mechanically suppressing lithium dendrite growth by functioning as a reversible, self-reinforcing protective layer on lithium anode. In contrast, without such phase transformation, conventional polymer electrolytes have a small modulus $< 10 \text{ MPa}$, leading to fast lithium dendrite growth. This strategy is universal and effective with different salt and plasticizers. By utilizing this unexpected mechano-chemical coupling mechanism, we successfully demonstrated $\text{LiFePO}_4/\text{PEO}/\text{Li}$ cells with 200 stable cycles, while cells without this mechanism failed quickly within 10 cycles. This study shows that phase transformation can be used as a new strategy to suppress lithium dendrite. This strategy is compatible with state-of-the-art battery materials and manufacturing processes without extra

needs to control the conformability of protective layers in previous literature. It will facilitate the development of solid polymer electrolyte-based lithium metal batteries with enhanced thermal stability and high energy density.

Acknowledgement

We acknowledge seed funding support from Columbia University's Research Initiatives in Science & Engineering (RISE) award, and Columbia SEAS Interdisciplinary Research Seed (SIRS) funding. Y. Y. acknowledge the support from the Air Force Office of Scientific Research (FA9550-18-1-0410). W. M. and Y. M. acknowledge the support from National Science Foundation (Grant No. 1904684). L. C. and Z. L. acknowledge the support from the Department of Energy, Office of Energy Efficiency and Renewable Energy (EERE), under the Award #DE-EE0007803 from the Battery Material Research (BMR) Program. X. C. and H. W. thank the support of the Office of Naval Research (ONR) under Grand No. N00014-18-1-2492. We also want to thank Prof. William Goddard at Caltech for his kind suggestions for this work.

References

1. Cheng, X.-B., Zhang, R., Zhao, C.-Z., Zhang, Q. Toward safe lithium metal anode in rechargeable batteries: a review. *Chem. Rev.* **117**, 10403-10473 (2017).
2. Lin, D., Liu, Y., Cui, Y. Reviving the lithium metal anode for high-energy batteries. *Nat. Nano.* **12**, 194 (2017).
3. Albertus, P., Babinec, S., Litzelman, S., Newman, A. Status and challenges in enabling the lithium metal electrode for high-energy and low-cost rechargeable batteries. *Nat. Energy* **3**, 16-21 (2018).
4. Li, N. W., Yin, Y. X., Yang, C. P., Guo, Y. G. An artificial solid electrolyte interphase layer for stable lithium metal anodes. *Adv. Mater.* **28**, 1853-1858 (2016).
5. Basile, A., Bhatt, A. I., O'Mullane, A. P. Stabilizing lithium metal using ionic liquids for long-lived batteries. *Nat. Commun.* **7**, 1-11 (2016).
6. Han, F., *et al.* High electronic conductivity as the origin of lithium dendrite formation within solid electrolytes. *Nat. Energy* **4**, 187-196 (2019).
7. Wang, X., *et al.* Stress-driven lithium dendrite growth mechanism and dendrite mitigation by electroplating on soft substrates. *Nat. Energy* **3**, 227-235 (2018).
8. Xiao, J. How lithium dendrites form in liquid batteries. *Science* **366**, 426-427 (2019).

9. Liu J, *et al.* Pathways for practical high-energy long-cycling lithium metal batteries. *Nat. Energy* **4**, 180-186 (2019).
10. Xu, K. Nonaqueous liquid electrolytes for lithium-based rechargeable batteries. *Chem. Rev.* **104**, 4303-4418 (2004).
11. Tikekar, M. D., Choudhury, S., Tu, Z., Archer, L. A. Design principles for electrolytes and interfaces for stable lithium-metal batteries. *Nat. Energy* **1**, 16114 (2016).
12. Ren X, *et al.* Localized high-concentration sulfone electrolytes for high-efficiency lithium-metal batteries. *Chem* **4**, 1877-1892 (2018).
13. Chen, S., *et al.* High-Voltage Lithium-Metal Batteries Enabled by Localized High-Concentration Electrolytes. *Adv. Mater.* **30**, 1706102 (2018).
14. Lu, Q., *et al.* Dendrite-Free, High-Rate, Long-Life Lithium Metal Batteries with a 3D Cross-Linked Network Polymer Electrolyte. *Adv. Mater.* **29**, 1604460 (2017).
15. Panday, A., *et al.* Effect of molecular weight and salt concentration on conductivity of block copolymer electrolytes. *Macromolecules* **42**, 4632-4637 (2009).
16. Stone, G., *et al.* Resolution of the modulus versus adhesion dilemma in solid polymer electrolytes for rechargeable lithium metal batteries. *J. Electrochem. Soc.* **159**, A222-A227 (2012).
17. Hess, S., Wohlfahrt-Mehrens M, Wachtler M. Flammability of Li-ion battery electrolytes: flash point and self-extinguishing time measurements. *J. Electrochem. Soc.* **162**, A3084-A3097 (2015).
18. Li, D., Fang, W., Xing, Y., Guo, Y., Lin, R. Effects of dimethyl or diethyl carbonate as an additive on volatility and flash point of an aviation fuel. *J. Hazard. Mater.* **161**, 1193-1201 (2009).
19. Catoire, L., Naudet, V. A. unique equation to estimate flash points of selected pure liquids application to the correction of probably erroneous flash point values. *J. Phys. Chem. Ref. Data* **33**, 1083-1111 (2004).
20. Li, S., *et al.* A superionic conductive, electrochemically stable dual-salt polymer electrolyte. *Joule* **2**, 1838-1856 (2018).
21. Maitra, M. G., Sinha, M., Mukhopadhyay, A. K., Middya, T. R., De, U., Tarafdar, S. Ion-conductivity and Young's modulus of the polymer electrolyte PEO-ammonium perchlorate. *Solid State Ion.* **178**, 167-171 (2007).
22. Geng, H., *et al.* Fabrication and properties of composites of poly (ethylene oxide) and functionalized carbon nanotubes. *Adv. Mater.* **14**, 1387-1390 (2002).
23. Klongkan, S., Pumchusak, J. Effects of nano alumina and plasticizers on morphology, ionic conductivity, thermal and mechanical properties of PEO-LiCF₃SO₃ solid polymer electrolyte. *Electrochim. Acta* **161**, 171-176 (2015).
24. Barai, P., Higa, K., Srinivasan, V. Lithium dendrite growth mechanisms in polymer electrolytes and prevention strategies. *Phys. Chem. Chem. Phys.* **19**, 20493-20505 (2017).
25. Brissot, C., Rosso, M., Chazalviel, J. N., Lascaud, S. *In Situ* Concentration Cartography in the Neighborhood of Dendrites Growing in Lithium/Polymer-Electrolyte/Lithium Cells. *J. Electrochem. Soc.* **146**, 4393-4400 (1999).
26. Liu, S., *et al.* Effect of nano-silica filler in polymer electrolyte on Li dendrite formation in Li / poly (ethylene oxide)-Li (CF₃SO₂)₂N / Li. *J. Power Sources* **195**, 6847-6853 (2010).

27. Ramesh, S., Winie, T., Arof, A. Investigation of mechanical properties of polyvinyl chloride–polyethylene oxide (PVC-PEO) based polymer electrolytes for lithium polymer cells. *Eur. Polym. J.* **43**, 1963-1968 (2007).
28. Fu, K. K., *et al.* Flexible, solid-state, ion-conducting membrane with 3D garnet nanofiber networks for lithium batteries. *Proc. Natl. Acad. Sci. U. S. A.* **113**, 7094-7099 (2016).
29. Zeng, X., *et al.* Commercialization of lithium battery technologies for electric vehicles. *Adv. Energy Mater.* **9**, 1900161 (2019).
30. Fang, C., *et al.* Quantifying inactive lithium in lithium metal batteries. *Nature* **572**, 511-515 (2019).
31. Li, Y., *et al.* Atomic structure of sensitive battery materials and interfaces revealed by cryo–electron microscopy. *Science* **358**, 506-510 (2017).
32. Zachman, M. J., Tu, Z., Choudhury, S., Archer, L. A., Kourkoutis L. F. Cryo-STEM mapping of solid–liquid interfaces and dendrites in lithium-metal batteries. *Nature* **560**, 345 (2018).
33. Bhattacharyya, R., Key, B., Chen, H., Best, A. S., Hollenkamp, A. F., Grey, C. P. *In situ* NMR observation of the formation of metallic lithium microstructures in lithium batteries. *Nat. Mater.* **9**, 504 (2010).
34. Chandrashekar, S., Trease, N. M., Chang, H. J., Du, L.-S., Grey, C. P., Jerschow, A.. ⁷Li MRI of Li batteries reveals location of microstructural lithium. *Nat. Mater.* **11**, 311 (2012).
35. Zhang, L., *et al.* Lithium whisker growth and stress generation in an in situ atomic force microscope–environmental transmission electron microscope set-up. *Nat. Nano.*, 1-5 (2020).
36. Chen, Y., *et al.* Li metal deposition and stripping in a solid-state battery via Coble creep. *Nature* **578**, 251-255 (2020).
37. Yan, Y., Cheng, C., Zhang, L., Li, Y., Lu, J. Deciphering the Reaction Mechanism of Lithium-Sulfur Batteries by *In Situ / Operando* Synchrotron-Based Characterization Techniques. *Adv. Energy Mater.* **9**, 1900148 (2019).
38. Cao, C., Shyam, B., Wang, J., Toney, M. F., Steinrück, H.-G.. Shedding X-ray Light on the Interfacial Electrochemistry of Silicon Anodes for Li-Ion Batteries. *Acc. Chem. Res.* **52**, 2673-2683 (2019).
39. Yu, S.-H., Huang, X., Brock, J. D., Abruña, H.. Regulating key variables and visualizing lithium dendrite growth: an *operando* X-ray study. *J. Am. Chem. Soc.* **141**, 8441-8449 (2019).
40. Cheng, Q., *et al.* *Operando* and three-dimensional visualization of anion depletion and lithium growth by stimulated Raman scattering microscopy. *Nat. Commun.* **9**, 2942 (2018).
41. Fleury, G., *et al.* Resolving the Framework Position of Organic Structure-Directing Agents in Hierarchical Zeolites via Polarized Stimulated Raman Scattering. *J. Phys. Chem. Lett.* **9**, 1778-1782 (2018).
42. Li, H., *et al.* Imaging Chemical Kinetics of Radical Polymerization with an Ultrafast Coherent Raman Microscope. *Adv. Sci.*, 1903644 (2020).
43. Freudiger, C. W., *et al.* Label-free biomedical imaging with high sensitivity by stimulated Raman scattering microscopy. *Science* **322**, 1857-1861 (2008).
44. Bai, P., Li, J., Brushett, F. R., Bazant, M. Z. Transition of lithium growth mechanisms in liquid electrolytes. *Energy Environ. Sci.* **9**, 3221-3229 (2016).

45. Alarco, P.-J., Abu-Lebdeh, Y., Abouimrane, A., Armand, M. The plastic-crystalline phase of succinonitrile as a universal matrix for solid-state ionic conductors. *Nat Mater.* **3**, 476 (2004).
46. Brouillette, D., Irish, D. E., Taylor, N. J., Perron, G., Odziemkowski, M., Desnoyers, J. E. Stable solvates in solution of lithium bis(trifluoromethylsulfone) imide in glymes and other aprotic solvents: Phase diagrams, crystallography and Raman spectroscopy. *Phys. Chem. Chem. Phys.* **4**, 6063-6071 (2002).
47. Fengler, O., Ruoff, A. Vibrational spectra of succinonitrile and its [1,4-¹³C₂]-, [2,2,3,3-²H₄]- and [1,4-¹³C₂-2,2,3,3-²H₄]-isotopomers and a force field of succinonitrile. *Spectrochim. Acta A.* **57**, 105-117 (2001).
48. Miyazawa, T., Fukushima, K., Ideguchi, Y. Molecular vibrations and structure of high polymers. III. Polarized infrared spectra, normal vibrations, and helical conformation of polyethylene glycol. *J. Chem. Phys.* **37**, 2764-2776 (1962).
49. Sneddon IN. Boussinesq's problem for a rigid cone. In: *Mathematical Proceedings of the Cambridge Philosophical Society*. Cambridge University Press (1948).

Stabilizing Lithium Metal Anode by Ion Depletion-induced ... (2.50 MiB)

[view on ChemRxiv](#) • [download file](#)

Stabilizing Lithium Metal Anode by Ion Depletion-Induced Phase Transformation in Polymer Electrolytes

Qian Cheng,^{1,6} Yupeng Miao,^{2,6} Zhe Liu,³ James Borovilas,¹ Hanrui Zhang,¹ Shuwei Liu,¹ Haozhen Wang,⁴ Xi Chen,^{4,5} Long-Qing Chen,³ Wei Min,^{2*} Yuan Yang^{1*}

¹ Program of Materials Science and Engineering, Department of Applied Physics and Applied Mathematics, Columbia University, New York, NY 10027, USA

² Department of Chemistry, Columbia University, New York, NY, 10027, USA

³ Department of Materials Science and Engineering, The Pennsylvania State University, University Park, State College, PA 16802, USA.

⁴ Advanced Science Research Center (ASRC), City University of New York, 85 St. Nicholas Terrace, New York, NY, 10031 USA

⁵ Department of Chemical Engineering, The City College of New York, 160 Convent Avenue, New York, NY 10031, USA

⁶ These authors contributed equally

Correspondence: Y.Y. (yy2664@columbia.edu) or W.M. (wm2256@columbia.edu)

Abstract: Ion depletion in liquid electrolytes is widely accepted to promote dendrite growth in metal anodes due to enhanced local electrical field and magnified concentration fluctuation at the electrode/electrolyte interface. Here we report unexpected opposite behaviors in solid polymer electrolytes, showing that ion depletion leads to uniform lithium deposition. Such stabilization originates from ion depletion-induced phase transformation, which forms a new PEO-rich but salt/plasticizer-poor phase at the lithium/electrolyte interface, as unveiled by stimulated Raman scattering microscopy. This new phase leads a significantly higher Young's modulus (~2-3 GPa) than the bulk polymer electrolyte (< 10 MPa), which effectively suppresses dendrite growth. Further battery tests show that LiFePO₄/PEO/Li cells with such ion depletion-induced phase transformations can be reversibly cycled for 200 times, while cells without such transformation fail within only ten cycles, demonstrating the effectiveness of this strategy to stabilize the lithium anode.

Introduction

Lithium-metal batteries (LMBs) have attracted significant attention in recent years for next-generation energy storage with high energy density^{1, 2, 3}. Li metal anode has a theoretical capacity of 3860 mAh g⁻¹, ten times that of the conventional graphite anode, and an ultralow electrode potential (-3.04 V vs. standard hydrogen electrode / SHE). However, lithium deposition is prone to being non-uniform, leading to rough morphologies such as mossy and dendritic lithium^{4, 5, 6, 7}. Such uneven deposition not only results in a large electrode surface area which promotes side reactions with electrolyte and decreases coulombic efficiency and cycle life^{8, 9}, but also imposes potential safety hazards such as internal shorting and thermal runaway, especially in combination with conventional flammable liquid electrolytes (e.g. ethers and carbonates)^{10, 11, 12, 13}.

Polymer electrolytes are appealing for enhancing the thermal stability of LMBs as they are much more thermally stable than liquid electrolytes^{14, 15, 16}. For example, the flash points (f.p.) of poly (ethylene oxide) is 250 °C¹⁷, much higher than dimethyl carbonate (21.5 °C)¹⁸, 1,3-dioxolane (2 °C)¹⁹ and 1,2-dimethoxyethane (-2 °C)¹⁷ in liquid electrolytes. Polymer electrolytes are also compatible with conventional battery manufacturing processes and easy to scale up²⁰. Unfortunately, Young's moduli of PEO-based polymer electrolytes are typically in the range of 20 to 70 MPa^{21, 22, 23}, much lower than the proposed threshold of 1 GPa needed to suppress Li dendrites^{11, 24}. Hence, the fast growth of Li dendrites in polymer electrolytes is widely observed in literature^{24, 25, 26}, and Supplementary Movie 1. The dendrite growth becomes even more severe with the introduction of plasticizers for enhancing ionic conductivity, as they further soften the electrolyte^{23, 27}. This issue is difficult to be fully resolved by ceramic additives,²⁸ since lithium dendrites can still penetrate through the interspace between ceramic fillers. Currently, Li dendrite growth remains one of the major challenges in polymer electrolyte-based LMBs.²⁹

Addressing this issue requires fundamental understanding of the embedded dynamic Li metal/polymer electrolyte interface, such as how Li⁺ heterogeneity evolves at the Li anode surface and how the Li anode interacts with solid electrolytes. While remarkable advances have been achieved recently in characterizing the Li anode and solid electrolyte interphase (SEI) in liquid electrolytes, such as cryo-transmission electron microscope (TEM),^{30, 31, 32} nuclear magnetic resonance (NMR),^{33, 34} *in-situ* and environmental TEM,^{35, 36} synchrotron,^{37, 38} and ambient pressure XPS³⁹, there is limited progress towards imaging the interaction between Li⁺ transport in the

electrolyte and Li dendrite growth. This arises from challenges in visualizing ions in the electrolyte, which not only has a low concentration (0.01-2 M), but also possesses fast dynamics (diffusivity of $\sim 10^{-7}$ - 10^{-6} cm² s⁻¹) compared to solid electrodes (10-50 M, and $<10^{-9}$ cm² s⁻¹). Hence, ultra-high chemical sensitivity (~ 1 -10 mM), high speed (~ 1 s/image), and fine spatial resolution (<1 μ m) are simultaneously required to image the electrolyte, especially during ion depletion. Such resolutions and sensitivity are beyond the capability of conventional characterization tools.

Recently we utilized stimulated Raman scattering (SRS) microscopy to image ion transport profile in liquid electrolytes, which simultaneously offers high sensitivity (< 1 mM), fast imaging speed (~ 2 μ s per pixel), and fine spatial resolution (down to 300 nm)^{40, 41, 42}. SRS microscopy uses two temporally and spatially synchronized laser beams with an energy difference equal to that of the target bond's vibrational mode. The synergy of the two beams amplifies the otherwise weak vibrational signal by up to 10^8 times. It thus enables the desired resolutions, imaging speed, and sensitivity (**Fig. 1a**, Supplementary Fig. 1).⁴³ Using this emerging microscopy, we visualized for the first time the heterogeneity of ion depletion in liquid electrolytes and how it correlated with lithium dendrite growth.⁴⁰ We observed that ion depletion at the Li/electrolyte interface led to faster dendrite growth due to the enhanced electrical field and larger concentration heterogeneity, which agreed with theoretical predictions.^{1, 44}

In this report, we further explored the solid polymer electrolyte/electrode interaction and observed unexpected opposite phenomena. Instead of promoting dendrite formation, ion depletion strongly suppressed dendrite growth in PEO electrolytes and led to reversible lithium plating and stripping. Further analysis unveiled that this unusual behavior originated from an ion depletion-induced phase transformation in the polymer electrolyte and subsequent mechano-chemical coupling inside (**Fig. 1b**). Once ions deplete, a new PEO-rich phase was formed at the lithium/electrolyte interface with a high modulus ~ 1 -3 GPa, as measured by atomic force microscopy (AFM). Such a high modulus suppressed dendrite growth and led to uniform lithium deposition. Based on this discovery, we developed a PEO electrolyte with an optimal composition (EO/Li = 6, ~ 1.6 M Li salt), which showed stable cycling over 200 times in an LFP/PEO/Li cell at 38 °C. In contrast, LFP/PEO/Li cells with concentrated electrolyte (EO/Li = 3, ~ 2.7 M Li salt) failed quickly after 10 cycles due to the rapid growth of lithium dendrites and dramatically

increased impedance. This work proposes a new strategy for using self-forming mechanically strong phases to stabilize the lithium metal anode in solid-polymer-electrolyte-based LMBs.

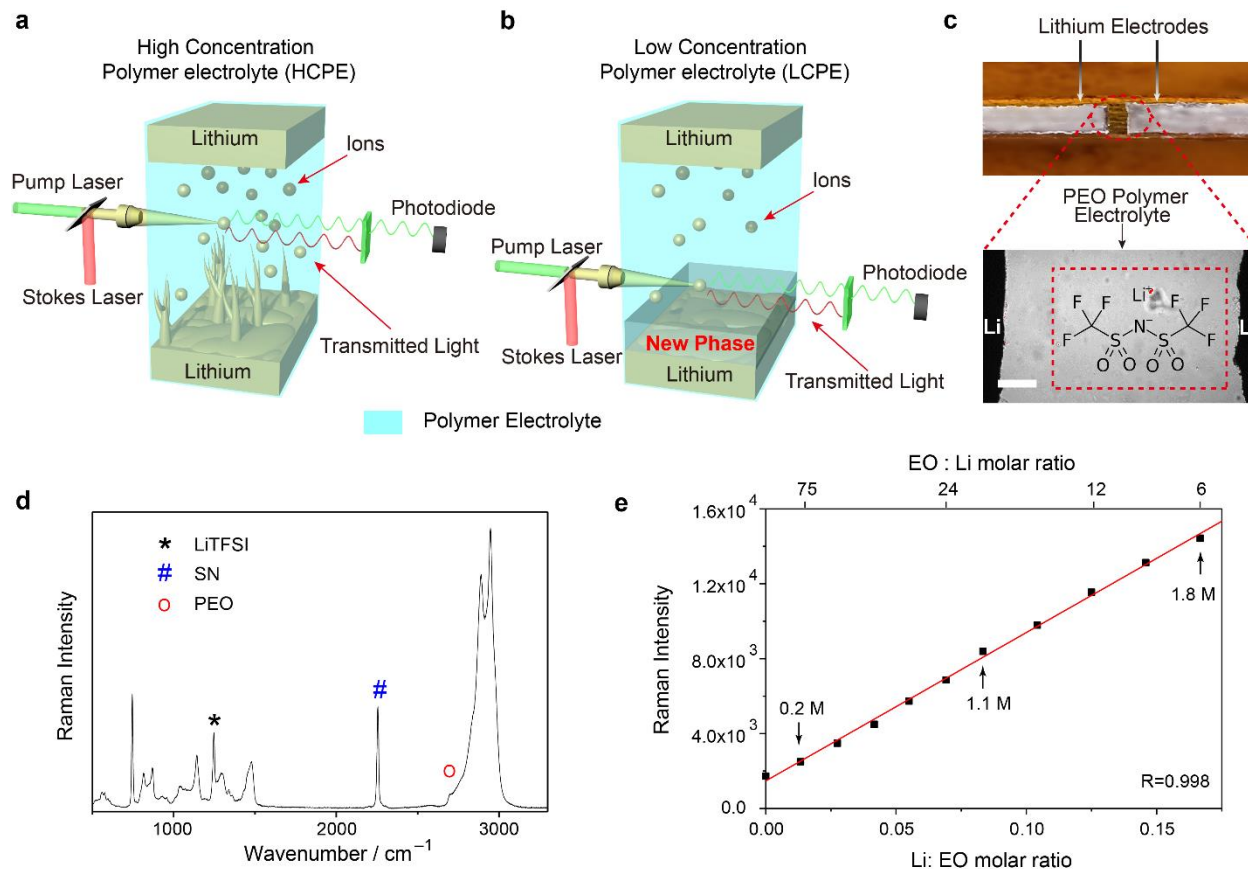


Figure 1. The schematics of *operando* SRS imaging of the Li/PEO electrolyte interface. The schematics of SRS observations on **a**, high concentration polymer electrolyte (HCPE) and **b**, low concentration polymer electrolyte (LCPE) in Li/Li cells. In LCPE, the ion depletion-induced phase transformation leads to a mechanically strong PEO-rich phase at the lithium/electrolyte interface, which helps suppress lithium dendrites. **c**, the bright field of a Li/PEO/Li cell *in operando*. The upper picture shows the structure of the cell, while the lower one shows a zoom-in image under the microscope. **d**, the Raman spectrum of LCPE, where signature peaks for LiTFSI, SN, and PEO are labeled. The corresponding composition of LCPE is EO: Li: SN = 12: 1: 2.64. **e**, the plot of Raman intensity of the LiTFSI peak at 1245 cm^{-1} versus the Li: EO ratio in PEO electrolytes with 40 wt% SN, showing good linearity. The points of 1.1 M and 1.8 M LiTFSI correspond to LCPE and HCPE, respectively.

Results

SRS imaging of Li / solid polymer electrolyte interaction. Home-made parallel cells were used to visualize the Li / PEO electrolyte interaction via SRS microscopy (**Fig. 1c**). In this cell, the PEO electrolyte filled in the gap between two pieces of lithium, and all components were sandwiched between two glass slides and sealed by epoxy. The distance between two electrodes was typically ~ 0.5 mm. The PEO electrolyte contained lithium bis(trifluoromethanesulfonyl) imide (LiTFSI) as the salt and succinonitrile (SN) as the plasticizer⁴⁵ to enhance ionic conductivity and enable operation at room temperature. Wavenumbers at 1245 cm^{-1} (CF_3 stretching),⁴⁶ 2250 cm^{-1} ($\text{C}\equiv\text{N}$ stretching),⁴⁷ and 2800 cm^{-1} (C-H stretching with combination vibration)⁴⁸ were selected for SRS imaging of LiTFSI, SN and PEO, respectively (**Fig. 1d**). Due to the requirement of electroneutrality, $[\text{Li}^+]$ could be considered to be equal to $[\text{TFSI}^-]$, even at the nanoscale (Supplementary Note 2), with an error smaller than 0.1 mM .⁴⁰ Therefore, $[\text{TFSI}^-]$ was measured to represent the local $[\text{Li}^+]$. The Raman intensity of TFSI^- is proportional to its concentration. Hence the Raman signal can be easily converted to chemical concentrations (**Fig. 1e**). The chemical sensitivity of LiTFSI was calculated to be 0.012 M .

Lithium growth in PEO electrolytes with high and low concentration. As two representatives, the high-concentration polymer electrolyte (HCPE) and the low-concentration polymer electrolyte (LCPE) were studied with EO: Li: SN = 12: 2: 2.64 and 12: 1: 2.64 in molarity, respectively, which corresponded to 1.8 M LiTFSI and 2.4 M SN for HCPE, and 1.1 M LiTFSI and 2.9 M SN for LCPE. The weight ratios of SN to PEO were fixed at 40% in both cases. Their ionic conductivities are $1.7 \times 10^{-4}\text{ S cm}^{-1}$ (HCPE) and $1.0 \times 10^{-4}\text{ S cm}^{-1}$ (LCPE) at room temperature (RT), respectively (Supplementary Fig. 2). Due to the relatively low ionic conductivities at RT, a current density of 0.5 mA cm^{-2} was applied.

In the case of HCPE (**Fig. 2a & Supplementary Movie 2**), the applied current gradually depleted $[\text{Li}^+]$ on the lithium surface ($[\text{Li}^+]_{0\ \mu\text{m}}$) from 1.8 M at $t = 0$ to 1.2 M at $t = 27\text{ min}$, after which $[\text{Li}^+]_{0\ \mu\text{m}}$ remained at $\sim 1.2\text{ M}$ in a steady state (**Fig. 2b & c**). Meanwhile, the lithium growth rate (ν) quickly increased from $0.27 \pm 0.18\ \mu\text{m min}^{-1}$ at $t = 0$ to $0.9 \pm 0.46\ \mu\text{m min}^{-1}$ at $t = 27\text{ min}$ (**Fig. 2d**). The growth was in the form of mossy lithium, and statistical analysis showed a normal distribution of ν (Supplementary Fig. 3a-c). Afterwards, ν was drastically increased to $\sim 1.5\ \mu\text{m min}^{-1}$ for the remaining time, leading to an ultrahigh porosity of 97%, indicating that the HCPE

could not suppress dendrite growth at all. A dual-peak normal distribution was observed at this stage (Supplementary Fig. 3d-h), where v was low in part of the surface ($< 1 \mu\text{m min}^{-1}$), but ultrahigh in other regions ($> 2 \mu\text{m min}^{-1}$), showing the heterogeneous dendrite growth on lithium electrode. This dual-peak mode may arise from SEI properties and non-uniform depletion of ions. These results shows that if no phase transformation occurs, ion depletion at the Li/polymer electrolyte interface promotes dendrite growth (Supplementary Movie 2), similar to our previous observations in gel electrolyte.⁴⁰

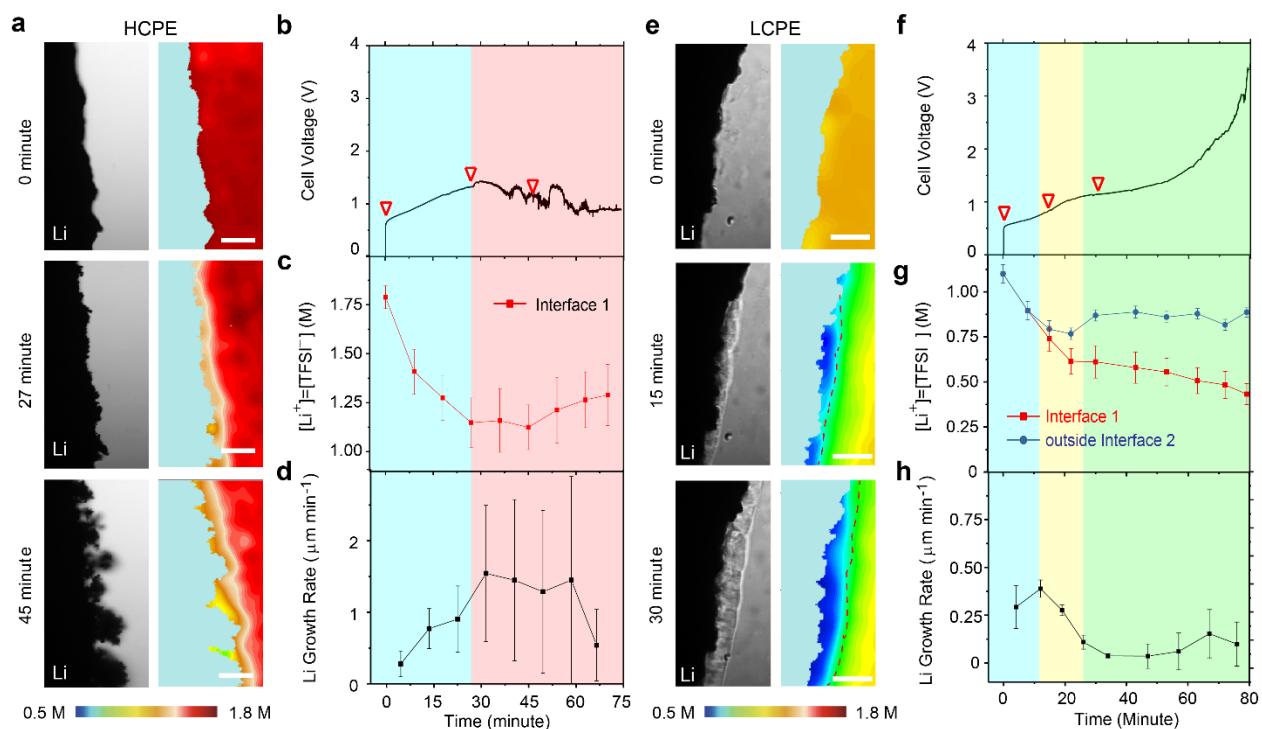


Fig. 2. Lithium growth at the lithium/PEO electrolyte interface with HCPE or LCPE. **a-d**, lithium dendrite growth in HCPE. **a**, the bright field and corresponding SRS images of $[\text{Li}^+] = [\text{TFSI}^-]$ at three representative stages. **b**, the voltage profile of the Li/Li cell. **c**, $[\text{Li}^+] = [\text{TFSI}^-]$ versus time, and **d**, the lithium growth rate (v) versus time. Interface 1 refers to the boundary between the lithium electrode and the PEO electrolyte. **e-h**, lithium growth in LCPE. **e**, the bright field and SRS images of $[\text{Li}^+]$ at three representative moments. **f**, the voltage profile of the Li/Li cell. The yellow shading corresponds to the appearance of the PEO-rich phase and the green shading indicates the regime where the PEO-rich phase has covered the entire lithium surface. **g**, $[\text{Li}^+] = [\text{TFSI}^-]$ versus time, and **h**, the lithium growth rate (v) versus time. Interface 2 refers to the boundary between the new PEO-rich phase and the isotropic bulk polymer electrolyte, as marked by dash lines in SRS images in **e**. Scale bars are $50 \mu\text{m}$. Zoom-in SRS images of **a** & **e** are shown in Supplementary Fig. 4.

In contrast to the conventional behaviors observed in HCPE, we find that ion depletion in LCPE induced a phase transformation process at the lithium/electrolyte interface that unexpectedly suppressed lithium dendrite growth, as observed by both SRS and bright-field (BF) images (**Fig. 2e** & Supplementary Movie 2). First, the new phase appeared as the blue color region in SRS and granular-like region in BF, which was confirmed by the spontaneous Raman spectrum (Supplementary Fig. 5). This new phase had a much lower [LiTFSI] than that in the isotropic bulk LCPE, as shown by the contrast between [LiTFSI] at the Li/electrolyte interface (interface 1), and [LiTFSI] outside the boundary between the new phase and the isotropic bulk electrolyte (interface 2). This difference increased from 0.79 M vs. 0.74 M at $t = 15$ min, to 0.87 M vs. 0.61 M at $t = 30$ min, and 0.89 M vs. 0.43 M at $t = 79$ min (**Fig. 2g**). Further study showed that the new phase was also poor in SN, [SN] was only ~ 1.8 M at the interface, compared to 3.8 M outside the interface 2 (Supplementary Fig. 6 and 7).

The appearance of this new phase unexpectedly but effectively suppressed the growth of lithium dendrites. Although the lithium dendrite growth was observed at $t = 0$ with v of $\sim 0.3 \mu\text{m min}^{-1}$ (87% porosity), v quickly dropped to $0.048 \mu\text{m/min}$ at $t = 30$ min after the initial formation of PEO-rich phase (**Fig. 2h**), equivalent to a porosity of 16%. At this stage, the PEO-rich phase progressively formed on the lithium metal surface. After the new phase fully covered the Li metal surface, the average v from 30 min to 63 min was only $0.044 \mu\text{m min}^{-1}$, which corresponded to a low porosity of 9.2%, about one thirtieth of that in HCPE, indicating a dense and uniform lithium deposition. Such behavior is not only self-forming but also self-reinforcing during ion depletion. For example, if Li dendrite grows fast at a certain location, the local current density will increase and lead to faster ion depletion and hence thicker new PEO-rich phase, which in turn suppresses dendrite growth (Supplementary Movie 1, LCPE). This active protection mechanism is distinct from other conventional passive protective layers, which requires perfect uniformity and durability. This suppression mechanism has not been reported in the literature, to the best of the authors' knowledge. This dynamic phase transformation and dendrite suppression are illustrated in Supplementary Movie 2.

The suppression mechanism and underlying mechano-chemical coupling. To understand how the new PEO-rich phase formed and suppressed dendrite growth, we first constructed the ternary phase diagram of PEO-LiTFSI-SN with the assistance of SRS (**Fig. 3a**), as it could measure the

composition of each phase in a high-throughput fashion. The phase diagram illustrates a single-phase isotropic zone (I-zone) in the middle (orange), and three two-phase regions at the corners (white & contour region). Representative SRS images of each region are shown in Supplementary Fig. 8. As shown in **Fig. 3a**, the composition of HCPE is at the center of the I-zone. When a low-to-mid-level current is applied, it progressively reduces [LiTFSI] on the lithium metal surface (Path A in **Fig. 3a**). Due to the high salt concentration in HCPE, the electrolyte composition at the Li/electrolyte interface remains within the I-zone during ion depletion, and thus no phase transformation occurred. In contrast, the composition of LCPE is close to the boundary between the single-phase I-zone and the two-phase region, making it susceptible to undergoing a phase transformation in response to ion depletion (Path B in **Fig. 3a**), since forming two phases is thermodynamically more stable than staying in one phase. This phase transformation reduces not only [LiTFSI], but also [SN] in the new phase, as confirmed by the redistribution of [SN] during the phase transformation (Supplementary Movie 3 and Supplementary Fig. 6 & 7).

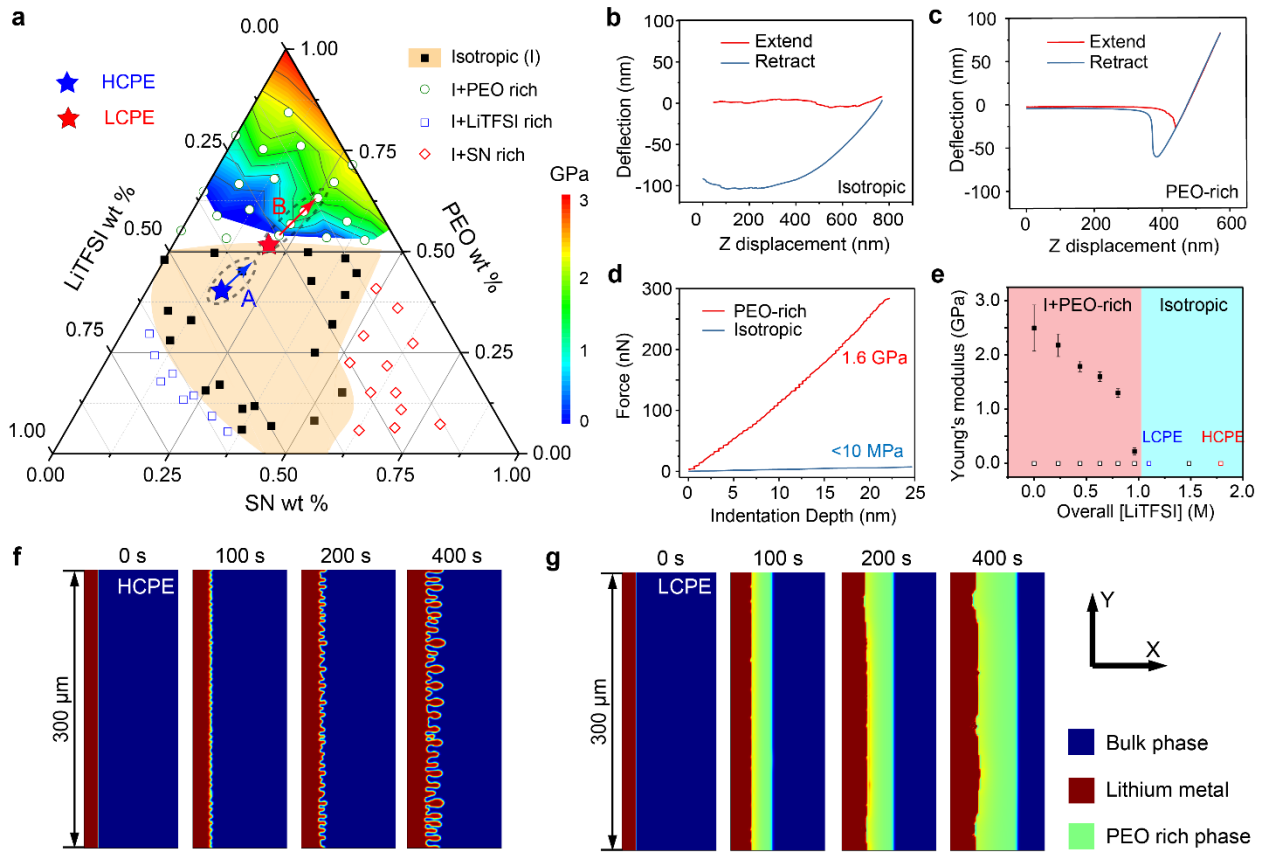


Fig. 3. The phase diagram and the mechanical properties of PEO-LiTFSI-SN polymer electrolytes. a, the ternary PEO-LiTFSI-SN phase diagram in weight percentage. The orange color marks the region of the

isotropic single-phase region, while other regions represent two phases. The rainbow color at the top of the triangle is the contour of Young's moduli of as-formed PEO-rich phases at corresponding compositions in the phase diagram. **b** & **c**, the AFM extending and retraction force curves of **b**, the isotropic bulk phase (I-zone, HCPE). No cantilever deformation is detected. **c**, the as-formed PEO-rich phase with a composition of 0.52 M LiTFSI and 2.6 M SN (See supplementary Table 1 for details). **d**, the corresponding force-indentation curves for samples in **b** and **c**. **e**, Young's moduli of the PEO-rich phase with different salt concentrations. The sample compositions are along the path A / B in **a**. All samples have the same SN/PEO ratio as HCPE and LCPE (40 wt%), but different [LiTFSI]. The exact composition of each phase is listed in Supplementary Table 1. The solid and empty squares show Young's moduli of the PEO-rich phase and the isotropic bulk phases, respectively. **f-g**, phase-field simulations of Li electrodeposition in solid polymer electrolytes with **f**, high concentration (2 M salt) and **g**, low concentration (1 M salt) at 0.5 mA cm⁻².

The effective suppression of Li dendrites by the new PEO-rich phase is hypothesized to arise from mechano-chemical coupling during the phase transformation at the Li/electrolyte interface. To verify this, AFM was used to measure the Young's moduli of solid polymer electrolytes (SPE) with different compositions, including both the I-zone and the PEO-rich phase, and the results are superimposed onto the phase diagram in **Fig. 3a**. For the composition of the HCPE (1.8 M LiTFSI and 2.4 M SN), the approaching curve showed no deformation of the cantilever when the tip was pressed into the electrolyte, indicating that the electrolyte was very soft (**Fig. 3b**). Large cantilever deflection is detected during tip retraction, confirming that the tip was pressed inside HCPE and the electrolyte was sticky. All SPEs within the I-zone and the isotropic phase of SPEs in the two-phase regions in **Fig. 3a** displayed similar results (Young's modulus $E < 10$ MPa), indicating they could not mechanically suppress lithium dendrite growth. Conversely, a classic force curve was observed for the PEO-rich phase formed in SPE. The sample had an overall composition of 0.6 M LiTFSI and 3.3 M SN, and the PEO-rich phase inside contained 0.52 M LiTFSI and 2.6 M SN (**Fig. 3c**). Using the Sneddon model,⁴⁹ the corresponding E was 1.6 GPa, well beyond the threshold to suppress lithium dendrites in previous studies,²⁴ thus explaining why dendrite growth was suppressed in LCPE. The conductivity of the as-formed PEO-rich state is in the order of 10⁻⁵ S cm⁻¹, which still allows Li⁺ to shuttle (Supplementary Fig. 9).

To further understand mechano-chemical coupling at the Li/electrolyte interface, the composition-dependent mechanical properties of the PEO-rich phases in PEO electrolytes were systematically measured by AFM. As shown in **Fig. 3e**, the modulus of the PEO-rich phase quickly

risers to 1.2 and 1.8 GPa when [LiTFSI] is reduced to 0.80 and 0.44 M in the PEO-rich phase (see Supplementary Table 1 for exact compositions in PEO rich phase). Further contour on the Young's moduli of the PEO-rich phases in the I + PEO-rich two-phase region (**Fig. 3a**) shows that the modulus is typically above 1 GPa when [LiTFSI] is less than 0.8 M. The contour indicates that the mechanism of ion depletion-induced stabilization of lithium deposition is effective in a wide range of electrolyte compositions.

The proposed suppression mechanism is also supported by phase-field simulations which take the mechano-chemical coupling into account (Supplementary Note 3 and Supplementary Movie 4). Since no new phase was formed in HCPE, lithium dendrites grew fast in the soft isotropic bulk polymer electrolyte ($E = 10$ MPa, **Fig. 3f** & Supplementary Fig. 10a). In contrast, the rigid PEO-rich phase was formed ($E = 1.6$ GPa) once $[\text{Li}^+]$ was depleted below 0.85 M, effectively suppressing lithium dendrite growth (**Fig. 3g** & Supplementary Fig. 10b). The deposited lithium was largely uniform and the $[\text{Li}^+]$ heterogeneity was low on the lithium surface. These simulation results strongly agree with experimental observations, supporting the hypothesis that the formation of the PEO-rich phase with high Young's modulus suppresses dendrite growth.

Ion depletion-induced stabilization of Li anode in Li/Li and LFP/PEO/Li cells. With the understanding that the formation of a mechanically rigid PEO-rich phase can stabilize lithium deposition, we further examined the effectiveness of this strategy in repeated cycles. First, as a proof-of-concept experiment, 0.5 mA cm^{-2} was applied to a Li/PEO-LCPE/Li symmetric cell with a deposition capacity of 0.25 mAh cm^{-2} for 20 cycles at room temperature. As observed with the optical microscope (**Fig. 4a** & Supplementary Movie 5), no obvious lithium dendrites formed in the first deposition, and the lithium protrusions were frozen by the growing PEO-rich phase, leading to stable lithium deposition. During the lithium stripping, both the PEO-rich phase and lithium metal electrode shrank without forming any dead lithium. Upon cycling, the lithium surface moved forward slightly after 20 cycles, indicating that this suppression mechanism was effective upon multiple cycles. Further tests showed that such a reversible behavior could be achieved in a wide range of currents from 0.25 to 1 mA cm^{-2} (Supplementary Video 5). It should be noted that the PEO-rich phase sometimes did not fully disappear during lithium stripping, which is attributed to its disappearance being a kinetically slow process. In contrast, without the PEO-rich phase, fast dendrite growth was observed within the first several cycles for Li/Li cells with

HCPE, forming large amounts of dead lithium during the repeated stripping process (Fig. 4b & Supplementary Movie 5).

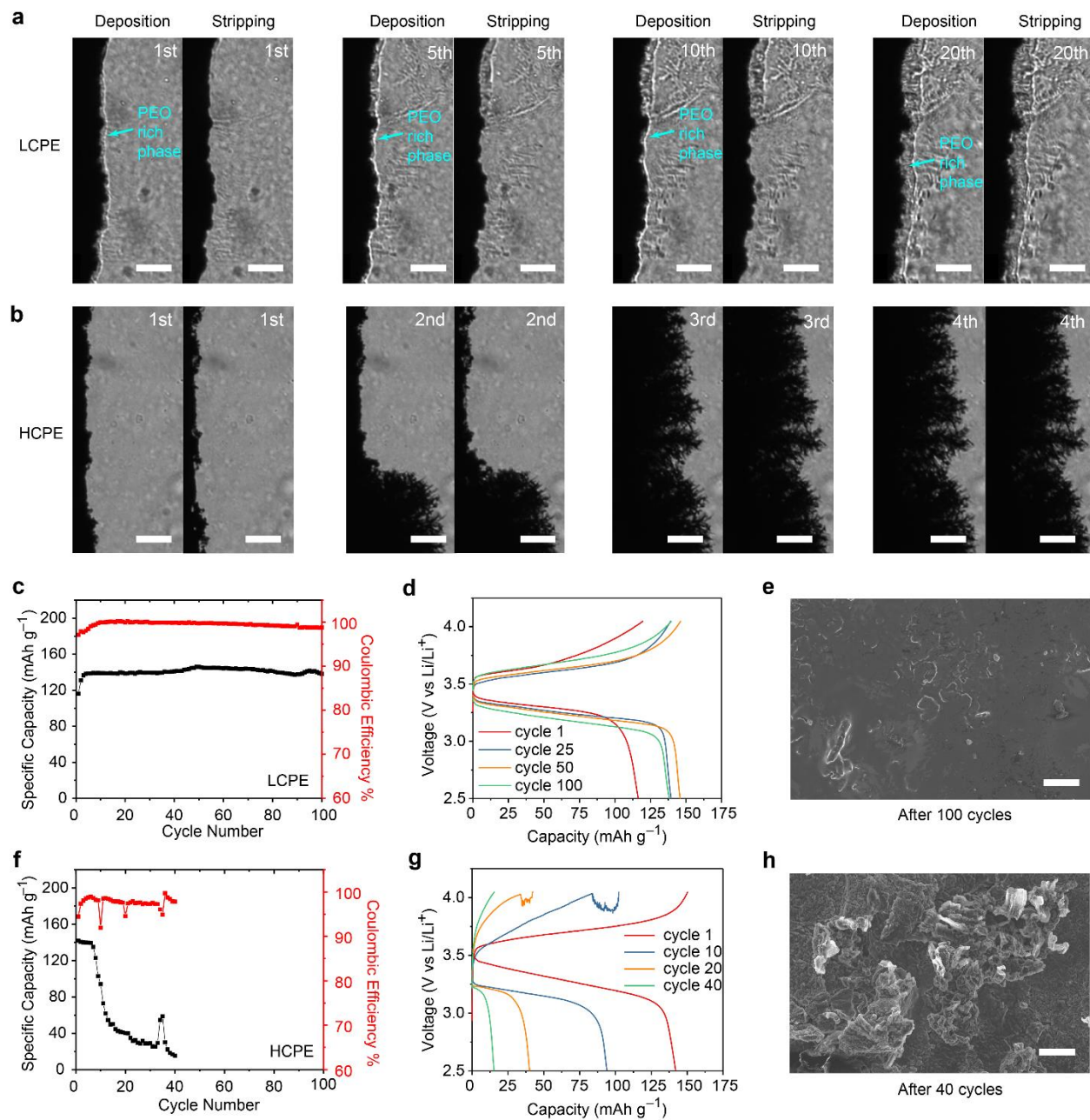


Fig 4. Cycling stability of the lithium metal anode in LCPE and HCPE. a-b, the bright-field images of the lithium electrodes during lithium plating and stripping in a. LCPE and b. HCPE. The scale bars are 100 μm . c, the cycling performance of $\text{LiFePO}_4/\text{Li}$ metal battery with LCPE and d, the corresponding voltage profiles. e, An SEM image of the lithium metal surface after 100 cycles. f, the cycling of $\text{LiFePO}_4/\text{Li}$ metal

battery with HCPE and **g**, the corresponding voltage profiles. **h**, An SEM image of the lithium metal surface after 40 cycles. The scale bars in **e** and **h** are 10 μm .

The effectiveness of this strategy was further demonstrated in LFP ($\sim 4 \text{ mg cm}^{-2}$)/PEO/Li cells at 0.25 C and 40 $^{\circ}\text{C}$. The PEO electrolyte was 100 μm -thick without a separator (Supplementary Fig. 11). Stable cycling was achieved with LCPE. The initial discharge capacity was 120 mAh g^{-1} and slowly increased to 141 mAh g^{-1} in the 4th cycle due to activation. After 100 cycles, the capacity remained at 140 mAh g^{-1} , corresponding to a retention of 99%. The average CE for cycle 5-100 is 99.6% (**Fig. 4c**). The voltage profile shows that the internal resistance only increases slightly and there is no sign of dendrite-induced short-circuit (**Fig. 4d**). SEM further revealed that the lithium metal surface was relatively flat after 100 cycles, with occasionally island-like morphology, demonstrating the effectiveness of the PEO-rich phase in suppressing lithium dendrites (**Fig. 4e**). On the other hand, the LFP/Li cell with HCPE quickly failed with the capacity dropping from 143 to 50.7 mAh g^{-1} after only 14 cycles (**Fig. 4f**). The voltage profile showed drastically increased overpotential, and the unstable voltage curve in charging suggests possible dendrite growth and micro-shorting (**Fig. 4g**). The average CE is only 97.4%, which probably arises from the prosperous growth of lithium dendrites, as validated by SEM imaging (**Fig. 4h**).

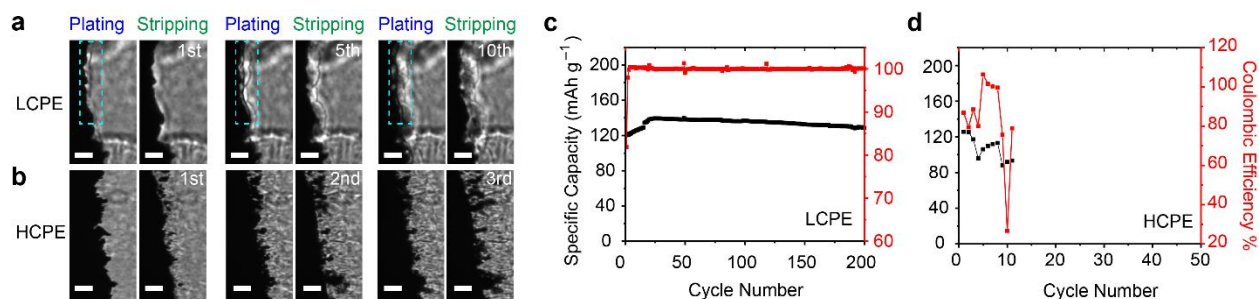


Fig 5. Cycling stability of the lithium metal anode in Li/Li cells and LFP/Li cells with PC/LiDFOB-LiBF₄ dual salt-based LCPE and HCPE. **a/b**, the bright-field images of the lithium electrodes in Li/Li cells with (a) LCPE and (b) HCPE at room temperature and 0.75 mA cm^{-2} . The scale bars are only 25 μm to better show the as-formed new PEO-rich phase (The dashed cyanic area). **c/d**, the cycling performance of LiFePO₄/Li metal batteries with (c) LCPE ($\text{EO/Li}^+ = 6$) and (d) HCPE ($\text{EO/Li}^+ = 3$) at 38 $^{\circ}\text{C}$. The current density is 0.3 mA/cm^2 . In both LCPE and HCPE, PC is used as the plasticizer and it is 90 wt % of PEO.

Such phase separation-induced dendrite suppression is universal in PEO electrolytes. In another PEO electrolyte of lithium difluoro(oxalato)borate (LiDFOB) and lithium tetrafluoroborate (LiBF₄) as salts and PC as plasticizer, a similar phenomenon was also observed. In this system, phase separation exists when EO/Li⁺ > 6 and it diminishes at EO/Li = 5.3 (Supplementary Fig. 12), therefore, a PC-based LCPE with EO/Li⁺ = 6 (2.9 mS cm⁻¹) was tested in a Li/Li cell at 0.75 mA cm⁻². A PEO-rich layer was clearly observed during lithium deposition and capable of suppressing lithium dendrites (**Fig. 5a** and Supplementary Movie 6). In contrast, phase separation was not observed in the PC-based HCPE with EO/Li⁺ = 3 (5.2 mS cm⁻¹), and obvious dendrites and dead lithium were formed (**Fig. 5b**). The effectiveness of the strategy was also demonstrated in full cells. In an LFP/PC-based LCPE/Li cell with 5 mg LFP cm⁻² and 40 μm thin lithium (**Fig. 5c**), the cell shows steady cycling over 200 cycles at 0.3 mA cm⁻² (122, 140 and 129 mAh g⁻¹ in cycle 1, 25 and 200, respectively). In contrast, when LCPE was replaced by HCPE, the cell dies after ten cycles due to dendrite-induced internal shorting (**Fig. 5d**). The corresponding voltage profiles are shown in Supplementary Fig. 13. Batteries with 10 mg LFP cm⁻² (1.3 mAh cm⁻²) and 40 μm lithium also showed stable cycling. The cell capacity is 116 mAh g⁻¹ in cycle 1, 131 mAh g⁻¹ in cycle 20 and 119 mAh g⁻¹ in cycle 80 (Supplementary Fig. 14). Details of electrolyte composition and fabrication process can be found in Supplementary Note 1.

Conclusion

The dynamic ion depletion, phase transformation in polymer electrolytes, and their correlations with lithium deposition were observed for the first time thanks to the high chemical, temporal, and spatial resolutions of SRS microscopy. We successfully unveil phase transformation in the polymer electrolytes induced by ion depletion and the formation of a new PEO-rich phase at the electrode/electrolyte interface. This new phase has a high Young's modulus of up to 3 GPa, which is effective in mechanically suppressing lithium dendrite growth by functioning as a reversible, self-reinforcing protective layer on lithium anode. In contrast, without such phase transformation, conventional polymer electrolytes have a small modulus < 10 MPa, leading to fast lithium dendrite growth. This strategy is universal and effective with different salt and plasticizers. By utilizing this unexpected mechano-chemical coupling mechanism, we successfully demonstrated LiFePO₄/PEO/Li cells with 200 stable cycles, while cells without this mechanism failed quickly within 10 cycles. This study shows that phase transformation can be used as a new strategy to

suppress lithium dendrite. This strategy is compatible with state-of-the-art battery materials and manufacturing processes without extra needs to control the conformability of protective layers in previous literature. It will facilitate the development of solid polymer electrolyte-based lithium metal batteries with enhanced thermal stability and high energy density.

Acknowledgement

We acknowledge seed funding support from Columbia University's Research Initiatives in Science & Engineering (RISE) award, and Columbia SEAS Interdisciplinary Research Seed (SIRS) funding. Y. Y. acknowledge the support from the Air Force Office of Scientific Research (FA9550-18-1-0410). W. M. and Y. M. acknowledge the support from National Science Foundation (Grant No. 1904684). L. C. and Z. L. acknowledge the support from the Department of Energy, Office of Energy Efficiency and Renewable Energy (EERE), under the Award #DE-EE0007803 from the Battery Material Research (BMR) Program. X. C. and H. W. thank the support of the Office of Naval Research (ONR) under Grand No. N00014-18-1-2492. We also want to thank Prof. William Goddard at Caltech for his kind suggestions for this work.

References

1. Cheng, X.-B., Zhang, R., Zhao, C.-Z., Zhang, Q. Toward safe lithium metal anode in rechargeable batteries: a review. *Chem. Rev.* **117**, 10403-10473 (2017).
2. Lin, D., Liu, Y., Cui, Y. Reviving the lithium metal anode for high-energy batteries. *Nat. Nano.* **12**, 194 (2017).
3. Albertus, P., Babinec, S., Litzelman, S., Newman, A. Status and challenges in enabling the lithium metal electrode for high-energy and low-cost rechargeable batteries. *Nat. Energy* **3**, 16-21 (2018).
4. Li, N. W., Yin, Y. X., Yang, C. P., Guo, Y. G. An artificial solid electrolyte interphase layer for stable lithium metal anodes. *Adv. Mater.* **28**, 1853-1858 (2016).
5. Basile, A., Bhatt, A. I., O'Mullane, A. P. Stabilizing lithium metal using ionic liquids for long-lived batteries. *Nat. Commun.* **7**, 1-11 (2016).
6. Han, F., *et al.* High electronic conductivity as the origin of lithium dendrite formation within solid electrolytes. *Nat. Energy* **4**, 187-196 (2019).
7. Wang, X., *et al.* Stress-driven lithium dendrite growth mechanism and dendrite mitigation by electroplating on soft substrates. *Nat. Energy* **3**, 227-235 (2018).
8. Xiao, J. How lithium dendrites form in liquid batteries. *Science* **366**, 426-427 (2019).

9. Liu J, *et al.* Pathways for practical high-energy long-cycling lithium metal batteries. *Nat. Energy* **4**, 180-186 (2019).
10. Xu, K. Nonaqueous liquid electrolytes for lithium-based rechargeable batteries. *Chem. Rev.* **104**, 4303-4418 (2004).
11. Tikekar, M. D., Choudhury, S., Tu, Z., Archer, L. A. Design principles for electrolytes and interfaces for stable lithium-metal batteries. *Nat. Energy* **1**, 16114 (2016).
12. Ren X, *et al.* Localized high-concentration sulfone electrolytes for high-efficiency lithium-metal batteries. *Chem* **4**, 1877-1892 (2018).
13. Chen, S., *et al.* High-Voltage Lithium-Metal Batteries Enabled by Localized High-Concentration Electrolytes. *Adv. Mater.* **30**, 1706102 (2018).
14. Lu, Q., *et al.* Dendrite-Free, High-Rate, Long-Life Lithium Metal Batteries with a 3D Cross-Linked Network Polymer Electrolyte. *Adv. Mater.* **29**, 1604460 (2017).
15. Panday, A., *et al.* Effect of molecular weight and salt concentration on conductivity of block copolymer electrolytes. *Macromolecules* **42**, 4632-4637 (2009).
16. Stone, G., *et al.* Resolution of the modulus versus adhesion dilemma in solid polymer electrolytes for rechargeable lithium metal batteries. *J. Electrochem. Soc.* **159**, A222-A227 (2012).
17. Hess, S., Wohlfahrt-Mehrens M, Wachtler M. Flammability of Li-ion battery electrolytes: flash point and self-extinguishing time measurements. *J. Electrochem. Soc.* **162**, A3084-A3097 (2015).
18. Li, D., Fang, W., Xing, Y., Guo, Y., Lin, R. Effects of dimethyl or diethyl carbonate as an additive on volatility and flash point of an aviation fuel. *J. Hazard. Mater.* **161**, 1193-1201 (2009).
19. Catoire, L., Naudet, V. A unique equation to estimate flash points of selected pure liquids application to the correction of probably erroneous flash point values. *J. Phys. Chem. Ref. Data* **33**, 1083-1111 (2004).
20. Li, S., *et al.* A superionic conductive, electrochemically stable dual-salt polymer electrolyte. *Joule* **2**, 1838-1856 (2018).
21. Maitra, M. G., Sinha, M., Mukhopadhyay, A. K., Middy, T. R., De, U., Tarafdar, S. Ion-conductivity and Young's modulus of the polymer electrolyte PEO-ammonium perchlorate. *Solid State Ion.* **178**, 167-171 (2007).
22. Geng, H., *et al.* Fabrication and properties of composites of poly (ethylene oxide) and functionalized carbon nanotubes. *Adv. Mater.* **14**, 1387-1390 (2002).
23. Klongkan, S., Pumchusak, J. Effects of nano alumina and plasticizers on morphology, ionic conductivity, thermal and mechanical properties of PEO-LiCF₃SO₃ solid polymer electrolyte. *Electrochim. Acta* **161**, 171-176 (2015).
24. Barai, P., Higa, K., Srinivasan, V. Lithium dendrite growth mechanisms in polymer electrolytes and prevention strategies. *Phys. Chem. Chem. Phys.* **19**, 20493-20505 (2017).
25. Brissot, C., Rosso, M., Chazalviel, J. N., Lascaud, S. *In Situ* Concentration Cartography in the Neighborhood of Dendrites Growing in Lithium/Polymer-Electrolyte/Lithium Cells. *J. Electrochem. Soc.* **146**, 4393-4400 (1999).
26. Liu, S., *et al.* Effect of nano-silica filler in polymer electrolyte on Li dendrite formation in Li / poly (ethylene oxide)-Li (CF₃SO₂)₂N / Li. *J. Power Sources* **195**, 6847-6853 (2010).

27. Ramesh, S., Winie, T., Arof, A. Investigation of mechanical properties of polyvinyl chloride–polyethylene oxide (PVC-PEO) based polymer electrolytes for lithium polymer cells. *Eur. Polym. J.* **43**, 1963-1968 (2007).
28. Fu, K. K., *et al.* Flexible, solid-state, ion-conducting membrane with 3D garnet nanofiber networks for lithium batteries. *Proc. Natl. Acad. Sci. U. S. A.* **113**, 7094-7099 (2016).
29. Zeng, X., *et al.* Commercialization of lithium battery technologies for electric vehicles. *Adv. Energy Mater.* **9**, 1900161 (2019).
30. Fang, C., *et al.* Quantifying inactive lithium in lithium metal batteries. *Nature* **572**, 511-515 (2019).
31. Li, Y., *et al.* Atomic structure of sensitive battery materials and interfaces revealed by cryo–electron microscopy. *Science* **358**, 506-510 (2017).
32. Zachman, M. J., Tu, Z., Choudhury, S., Archer, L. A., Kourkoutis L. F. Cryo-STEM mapping of solid–liquid interfaces and dendrites in lithium-metal batteries. *Nature* **560**, 345 (2018).
33. Bhattacharyya, R., Key, B., Chen, H., Best, A. S., Hollenkamp, A. F., Grey, C. P. *In situ* NMR observation of the formation of metallic lithium microstructures in lithium batteries. *Nat. Mater.* **9**, 504 (2010).
34. Chandrashekar, S., Trease, N. M., Chang, H. J., Du, L.-S., Grey, C. P., Jerschow, A.. ⁷Li MRI of Li batteries reveals location of microstructural lithium. *Nat. Mater.* **11**, 311 (2012).
35. Zhang, L., *et al.* Lithium whisker growth and stress generation in an in situ atomic force microscope–environmental transmission electron microscope set-up. *Nat. Nano.*, 1-5 (2020).
36. Chen, Y., *et al.* Li metal deposition and stripping in a solid-state battery via Coble creep. *Nature* **578**, 251-255 (2020).
37. Yan, Y., Cheng, C., Zhang, L., Li, Y., Lu, J. Deciphering the Reaction Mechanism of Lithium-Sulfur Batteries by *In Situ / Operando* Synchrotron-Based Characterization Techniques. *Adv. Energy Mater.* **9**, 1900148 (2019).
38. Cao, C., Shyam, B., Wang, J., Toney, M. F., Steinrück, H.-G.. Shedding X-ray Light on the Interfacial Electrochemistry of Silicon Anodes for Li-Ion Batteries. *Acc. Chem. Res.* **52**, 2673-2683 (2019).
39. Yu, S.-H., Huang, X., Brock, J. D., Abruña, H.. Regulating key variables and visualizing lithium dendrite growth: an *operando* X-ray study. *J. Am. Chem. Soc.* **141**, 8441-8449 (2019).
40. Cheng, Q., *et al.* *Operando* and three-dimensional visualization of anion depletion and lithium growth by stimulated Raman scattering microscopy. *Nat. Commun.* **9**, 2942 (2018).
41. Fleury, G., *et al.* Resolving the Framework Position of Organic Structure-Directing Agents in Hierarchical Zeolites via Polarized Stimulated Raman Scattering. *J. Phys. Chem. Lett.* **9**, 1778-1782 (2018).
42. Li, H., *et al.* Imaging Chemical Kinetics of Radical Polymerization with an Ultrafast Coherent Raman Microscope. *Adv. Sci.*, 1903644 (2020).
43. Freudiger, C. W., *et al.* Label-free biomedical imaging with high sensitivity by stimulated Raman scattering microscopy. *Science* **322**, 1857-1861 (2008).
44. Bai, P., Li, J., Brushett, F. R., Bazant, M. Z. Transition of lithium growth mechanisms in liquid electrolytes. *Energy Environ. Sci.* **9**, 3221-3229 (2016).

45. Alarco, P.-J., Abu-Lebdeh, Y., Abouimrane, A., Armand, M. The plastic-crystalline phase of succinonitrile as a universal matrix for solid-state ionic conductors. *Nat Mater.* **3**, 476 (2004).
46. Brouillette, D., Irish, D. E., Taylor, N. J., Perron, G., Odziemkowski, M., Desnoyers, J. E. Stable solvates in solution of lithium bis(trifluoromethylsulfone) imide in glymes and other aprotic solvents: Phase diagrams, crystallography and Raman spectroscopy. *Phys. Chem. Chem. Phys.* **4**, 6063-6071 (2002).
47. Fengler, O., Ruoff, A. Vibrational spectra of succinonitrile and its [1,4-¹³C₂]-, [2,2,3,3-²H₄]- and [1,4-¹³C₂-2,2,3,3-²H₄]-isotopomers and a force field of succinonitrile. *Spectrochim. Acta A.* **57**, 105-117 (2001).
48. Miyazawa, T., Fukushima, K., Ideguchi, Y. Molecular vibrations and structure of high polymers. III. Polarized infrared spectra, normal vibrations, and helical conformation of polyethylene glycol. *J. Chem. Phys.* **37**, 2764-2776 (1962).
49. Sneddon IN. Boussinesq's problem for a rigid cone. In: *Mathematical Proceedings of the Cambridge Philosophical Society*. Cambridge University Press (1948).

Stabilizing Lithium Metal Anode by Ion Depletion-induced ... (1.49 MiB)

[view on ChemRxiv](#) • [download file](#)

Supplementary Information for

Stabilizing Lithium Metal Anode by Ion Depletion-Induced Phase Transformation in Polymer Electrolytes

Qian Cheng,^{1, 6} Yupeng Miao,^{2,6} Zhe Liu,³ James Borovilas,¹ Hanrui Zhang,¹ Shuwei Liu,¹
Haozhen Wang,⁴ Xi Chen,^{4,5} Long-Qing Chen,³ Wei Min,^{2*} Yuan Yang^{1*}

¹ Program of Materials Science and Engineering, Department of Applied Physics and Applied Mathematics, Columbia University, New York, NY 10027, USA

² Department of Chemistry, Columbia University, New York, NY, 10027, USA

³ Department of Materials Science and Engineering, The Pennsylvania State University, University Park, State College, PA 16802, USA.

⁴ Advanced Science Research Center (ASRC), City University of New York, 85, St. Nicholas Terrace, New York, NY, 10031 USA

⁵ Department of Chemical Engineering, The City College of New York, 160 Convent Avenue, New York, NY 10031, USA

⁶ These authors contributed equally

Correspondence: Y.Y. (yy2664@columbia.edu) or W.M. (wm2256@columbia.edu)

Supplementary Movie 1. The comparison of lithium plating in HCPE and LCPE under the optical microscope.

Supplementary Movie 2. SRS/bright field images of lithium plating in HCPE and LCPE

Supplementary Movie 3. Continuous SRS images of [SN] change during lithium plating in LCPE.

Supplementary Movie 4. Phase-field simulation of lithium plating in HCPE/LCPE.

Supplementary Movie 5. Bright field video of lithium plating/stripping in LCPE/HCPE at 0.5 mA cm^{-2} , 0.25 mA cm^{-2} , 1 mA cm^{-2} .

Supplementary Movie 6. Bright-field images of lithium plating/stripping in PEO/LiDFOB+LiBF₄/PC electrolyte at 0.75 mA cm^{-2} .

Supplementary Note 1: Experimental Methods

Preparation of solid polymer electrolyte (SPE) precursors

To prepare LCPE / HCPE, 0.19 g / 0.38 g lithium bis (trifluoromethanesulfonyl) imide (LiTFSI, Gotion) was dissolved in 5 g acetonitrile (Sigma-Aldrich) along with 0.35 g poly (ethylene oxide) (Mw 600,000, Sigma Aldrich) and 0.14 g succinonitrile (SN, Tokyo Chemical Industry). Then the solutions were stirred overnight to form a translucent solution. SPEs with other compositions were prepared similarly and the PEO is typically 7 wt % of acetonitrile. For PC based LCPE / HCPE, the preparation procedure is similar. LiDFOB and LiBF₄ are mixed first with a molar ratio of 1:1, then the dual salts, PEO, and PC were dissolved in 5 g acetonitrile with a weight of 0.16 g / 0.32 g, 0.35 g, and 0.315 g for LCPE / HCPE, respectively.

Preparation of the lithium-lithium symmetric cells

40 μm thick of lithium foil and 50 μm thick of SPEs were used in the Li/Li symmetric cells while the horizontal gap between two lithium metal electrodes is $\sim 500 \mu\text{m}$. One layer of Kapton tape was laminated onto a glass slide, and two chambers ($\sim 1 \times 1 \text{ cm}$ for each) and a channel ($\sim 1 \times 6 \text{ mm}$) to connect two chambers were cut inside Kapton tapes. The lithium foil was cut to the desired size and soaked in dimethyl sulfoxide (DMSO) with 0.2 wt% H₃PO₄ solution for 1 min to form a thin Li₃PO₄ protective layer to isolate the contact between Li and acetonitrile in the SPE precursor above. Lithium electrodes were then placed to two ends of the chamber, and the precursor of SPE above was dropped between two Li electrodes and rest to evaporate acetonitrile. Finally, Cu foils with similar sizes were placed on the two ends of lithium as an external electrical contact, and a glass cover is placed on top of the Li/Li cell, followed by sealing with epoxy. The whole process is done in a glove box with O₂ and water level $< 0.1 \text{ ppm}$.

Preparation of the LFP-PEO-Li cells

For SN-based PEO electrolyte, LiFePO₄ (LFP) was selected as the cathode material due to its stability with the PEO electrolyte. LFP, carbon black, and polyvinylidene fluoride (PVDF) were mixed with a mass ratio of 8:1:1, then stirred in N-methyl-2-pyrrolidone (NMP) overnight to form a uniform slurry. Then the LFP slurry was coated on an Al foil using the doctor blade, followed by drying at 110°C for 12 hours. The mass loading of LFP is $\sim 4 \text{ mg cm}^{-2}$. Then the LFP electrodes were assembled with lithium metal as anode and LCPE/HCPE as the electrolyte

in an argon-filled glove box with both H₂O and O₂ below 0.1 ppm. A Kapton ring with a thickness of 100 μm was used to fixate the distance between the LFP electrode and lithium metal. The cells were tested at 40 °C, which enhances ionic conductivity but the formation of the new PEO-rich phase still occurs. The cells were rested for 15 minutes and 1 hour after each charging and the discharging step, respectively.

For PC-based PEO electrolyte, the preparation procedure is similar, except that 0.7 wt% of CNT was added into the LFP electrodes to achieve better rate performance at high mass loading (5 mg~ 10 mg). The electrode will be infiltrated with PEO/PC/dual salts electrolyte, then roll-pressed, and assembled with 40 μm thick lithium metal. The batteries are tested under 38 °C.

Electrochemical characterizations

All electrochemical tests, including galvanostatic charging and discharging, impedance measurements, were performed by either a Bio-logic SP150 or Biologic VMP3 potentiostat.

Stimulated and spontaneous Raman scattering microscopy

The detailed SRS setup has been previously reported by the authors.⁴⁰ Briefly, A commercial laser source (picoEmerald, Applied Physics & Electronics, Inc.) was used to generate both the Pump and Stokes beams with 6 ps pulse width and 80 MHz repetition rate. The wavelength of Stokes is fixed at 1064 nm while the Pump beam has a tunable wavelength between 720 nm to 990 nm achieved by an optical parametric oscillator (OPO). Notably, the Stokes beam is modulated at 8 MHz by a built-in electro-optical modulator. The two beams are spatially and temporally overlapped and coupled into a commercial confocal laser-scanning microscope (FV1200MPE, Olympus), then tightly focused on the sample with a 25× water objective (XLPlan N, N.A.=1.05, Olympus). After passing through the sample, two beams are collected by a high N.A.=1.4 condenser (Oil immersion, Olympus). The Stokes beam is filtered off with a high O.D. bandpass filter (890/220 CARS, Chroma Technology), while the Pump beam is focused and detected on a large area silicon photodiode (FDS1010, ThorLabs) with 64 V DC voltage. The current output is terminated by a 50 Ω terminator and demodulated by a lock-in amplifier (HF2LI, Zurich instrument). The X-output (i.e. Pump loss signal) generated by the amplifier is fed into the software interface (FV10, Olympus) as pixel intensity.

All spontaneous Raman spectra were acquired with a commercial Raman microscope (Xplora, Horiba Jobin Yvon). A 532 nm diode laser is used as excitation light and focused by a 50×, N.A.=0.75 air objective (MPlan N, Olympus). All spectra were obtained with 5 s acquisition time and 3 times averaging then processed with LabSpec 6 software.

Measurement of Young's modulus using Atomic Force Microscopy

Bruker Multimode 8 AFM was used in this study. The SPEs with thicknesses of $\sim 10 \mu\text{m}$ were coated on stainless steel plates. The AFM chamber was purged by dry N_2 prior to the tests. The spring constant, half angle and Poisson's ratio of AFM tips are $\sim 3 \text{ N/m}$, 15° , and 0.4, respectively. The force curve is fitted by the Sneddon model to get Young's modulus. The approaching curve in the extending line will be fitted first to determine the indentation start point, then the force can be calculated using cantilever deformation and fitted with indentation to get Young's modulus.

Supplementary Note 2. Theoretical Analysis of Electroneutrality in the electrolyte

In this paper, the electroneutrality does not mean the difference between [TFSI⁻] and [Li⁺] is zero; the difference is small enough to be neglected at given resolutions of SRS microscopy. We can consider a planar electrode:

According to Poisson's Equation for electrostatics, the electrical potential Φ and ionic distribution satisfy:

$$\nabla^2\Phi = -\frac{F}{\varepsilon\varepsilon_0}\sum_i z_i c_i \quad (1)$$

Where F is the Faraday constant (96485 C mol⁻¹), ε is the relative permittivity of electrolyte and ε_0 is the vacuum permittivity (8.85×10⁻¹² F m⁻¹), and z_i and c_i are charge number and concentration of all ions in the electrolyte. In our cell, the maximum voltage is 5 V, and the distance is around 500 μm. Even if we consider an extreme condition, in which the maximum gradient of an electrical field ($-\nabla^2\Phi$) is 5V μm⁻², and relative permittivity is 10, the difference in anion and cation concentration (C_+-C_-) is still < 5 μM. Therefore, Li⁺ can be reflected by TFSI⁻ outside the double layer region (Debye length is 48.7 nm for 5 μM LiTFSI) which is much less than our spatial resolution. More detailed experimental and simulation results can be found in **Fig. 2** in the authors' previous work.¹

Supplementary Note 3. Phase-field simulation

To simulate Li electrodeposition and the concurrent multiphase evolution in the lithium salts/plasticizer/PEO solid polymer electrolyte, we developed a phase-field model for a half-cell system incorporating diffusion, elasticity, and nonlinear Butler-Volmer kinetics. This model contains two phase-field order parameters, i.e. ξ and ϕ , to differentiate each phase by describing their relative mass densities: $\{\xi=1; \phi=0\}$ for Li metal, $\{\xi=0; \phi=1\}$ for PEO precipitate and $\{\xi=0; \phi=0\}$ for electrolyte. At each phase boundary, order parameters vary continuously between 1 and 0 to form a diffuse interface of finite thickness. The total free energy of the system, including local, interfacial, electrostatic and mechanical contributions, is written as

$$F = \int [f_{local}(\xi, \phi, \tilde{c}) + f_{grad}(\nabla \xi, \nabla \phi) + f_{mech}(\xi, \phi) + f_{elec}(c, \varphi)] dV$$

where $\tilde{c}_i = c_i/c_0$ is a set of dimensionless concentrations of species (e.g. $i = Li^{+i}$), where c_0 is the bulk concentration of the solid phase. φ is the electrostatic potential. We formulated the bulk energy density in

the standard reference state (Θ) as $f_{local} = f_0(\xi, \phi, c) + c_0 RT \sum_i \tilde{c}_i \ln \tilde{c}_i + \sum_i c_i \mu_i^\ominus$, where the local free

energy density $f_0(\xi, \phi) = W_1 \xi^2 (1 - \xi)^2 + W_2 \phi^2 (1 - \phi)^2 + \frac{A_3}{2} \xi^2 \phi^2 + f_i(\phi, c)$. Based on experimental

observation, PEO precipitates when salt concentration (c_i) falls below 85% of the original in the lean salt concentration (1 mol/L) electrolyte. Therefore, the energy density of electrolyte and PEO precipitate was

constructed as $f_i(\phi, c) = [1 - h(\phi)] f_l(c) + h(\phi) f_{PEO}(c)$, where the energy densities $f_l = A_1 (c - c_i)^2$ and

$f_{PEO}(c) = A_2 c^2$ were interpolated by function $h(\xi) = \xi^3 (10 - 15\xi + 6\xi^2)$. Considering the low salt

solubility in PEO, we set parameters to be $A_1 = \frac{1}{10} A_2 = 1$. The phenomenological parameters are set to

be $W_1 = W_2 = \frac{1}{3} A_3 = 1$, so that the equilibrium states are represented by the degenerate minima with

equal depth. The gradient energy density takes the form of $f_{grad} = \frac{1}{2} \kappa_\xi (\nabla \xi)^2 + \frac{1}{2} \kappa_\phi (\nabla \phi)^2$, where κ_ξ and

κ_ϕ are gradient energy coefficients associated with the surface/interface energies of Li metal and PEO

precipitate, respectively. The PEO phase is assumed isotropic and thus κ_ϕ is constant. The anisotropic Li

dendrite growth is governed by an orientation-dependent gradient energy coefficient

$\kappa_\xi(\theta) = \kappa_{Li} [1 + \delta \cos(\omega\theta)]$, where κ_{Li} is related to the Li metal surface energy, δ and ω are the strength

and mode of the anisotropy, and θ is the angle between the normal vector at the interface and the reference axis. Given the random interfacial orientation between Li metal and electrolyte/PEO phases, we

considered the isotropic elasticity in this study. The elastic energy density is written as $f_{mech} = \frac{1}{2} C_{ijkl} \varepsilon_{kl} \varepsilon_{ij}$, where the stiffness $C_{ijkl} = h(\xi) E_{ijkl}^\xi + h(\phi_i) E_{ijkl}^\phi + [1 - h(\xi) - h(\phi_i)] E_{ijkl}^l$ is expressed in term of interpolating function $h(\xi)$, and the elasticity tensors of Li metal (E_{ijkl}^ξ), PEO (E_{ijkl}^ϕ) and electrolyte (E_{ijkl}^l).

The electrostatic energy density is in the form of $f_{elec}(c, \varphi) = F \sum_i z_i c_i \varphi$, where F is Faraday constant and z_i is the valence of charged species. Therefore, the phase morphology evolution equation for the Li metal phase is governed by the Butler-Volmer kinetics coupled Allen-Cahn equation,

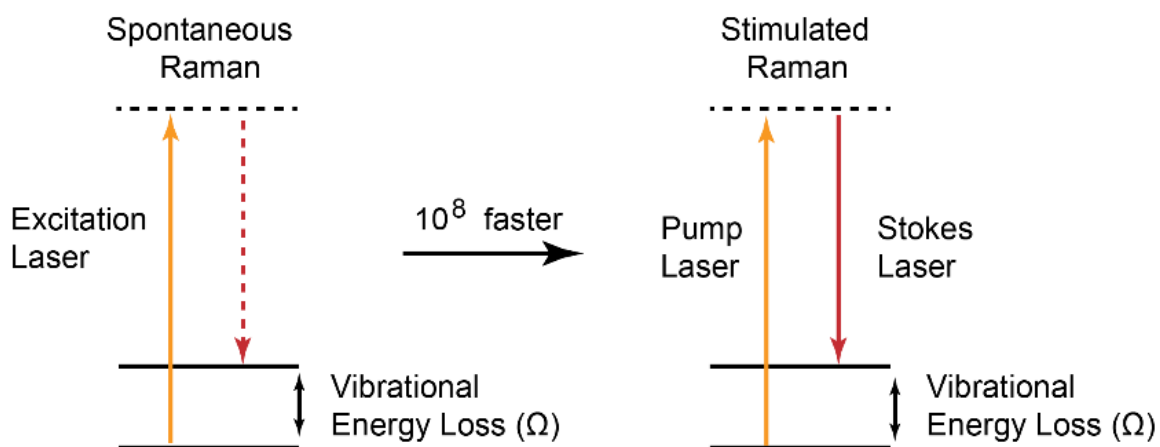
$$\frac{\partial \xi}{\partial t} = -L_\sigma^\xi \left(\frac{\partial f_0}{\partial \xi} - \kappa_\xi \nabla^2 \xi + \frac{\partial f_{mech}}{\partial \xi} \right) - L_\eta^\xi h'(\xi) \dot{c}$$

where L_σ^ξ and L_η^ξ are interface mobility and reaction constant, respectively. α is the Butler-Volmer symmetric factor and η is the overpotential. Likewise, the evolution equation for electrolyte phase is

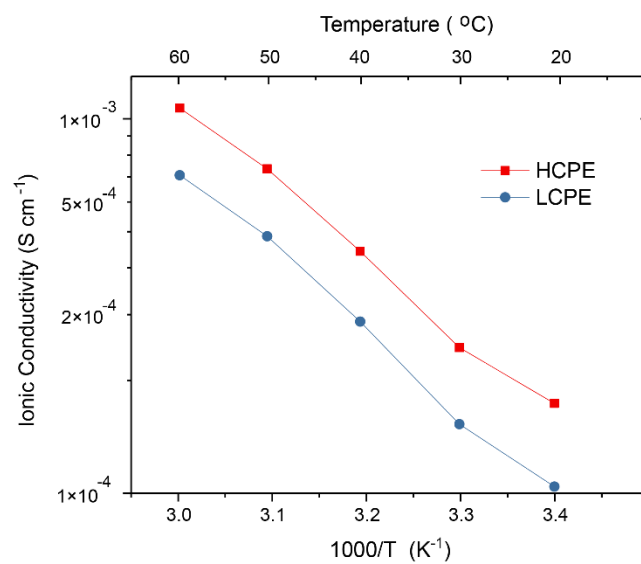
$$\frac{\partial \phi}{\partial t} = -M_\phi \left(\frac{\partial f_0}{\partial \phi} - \kappa_\phi \nabla^2 \phi + \frac{\partial f_{mech}}{\partial \phi} \right) + \delta_N$$

where M_ϕ is the interface mobility of solid electrolyte and δ_N is a Dirac delta function for PEO nucleation, which are detailed in reference.² The evolution of each phase-field was solved simultaneously with ionic diffusion, charge conservation, and mechanical equilibrium equations. The model details and parameter table are in references.²⁻⁴

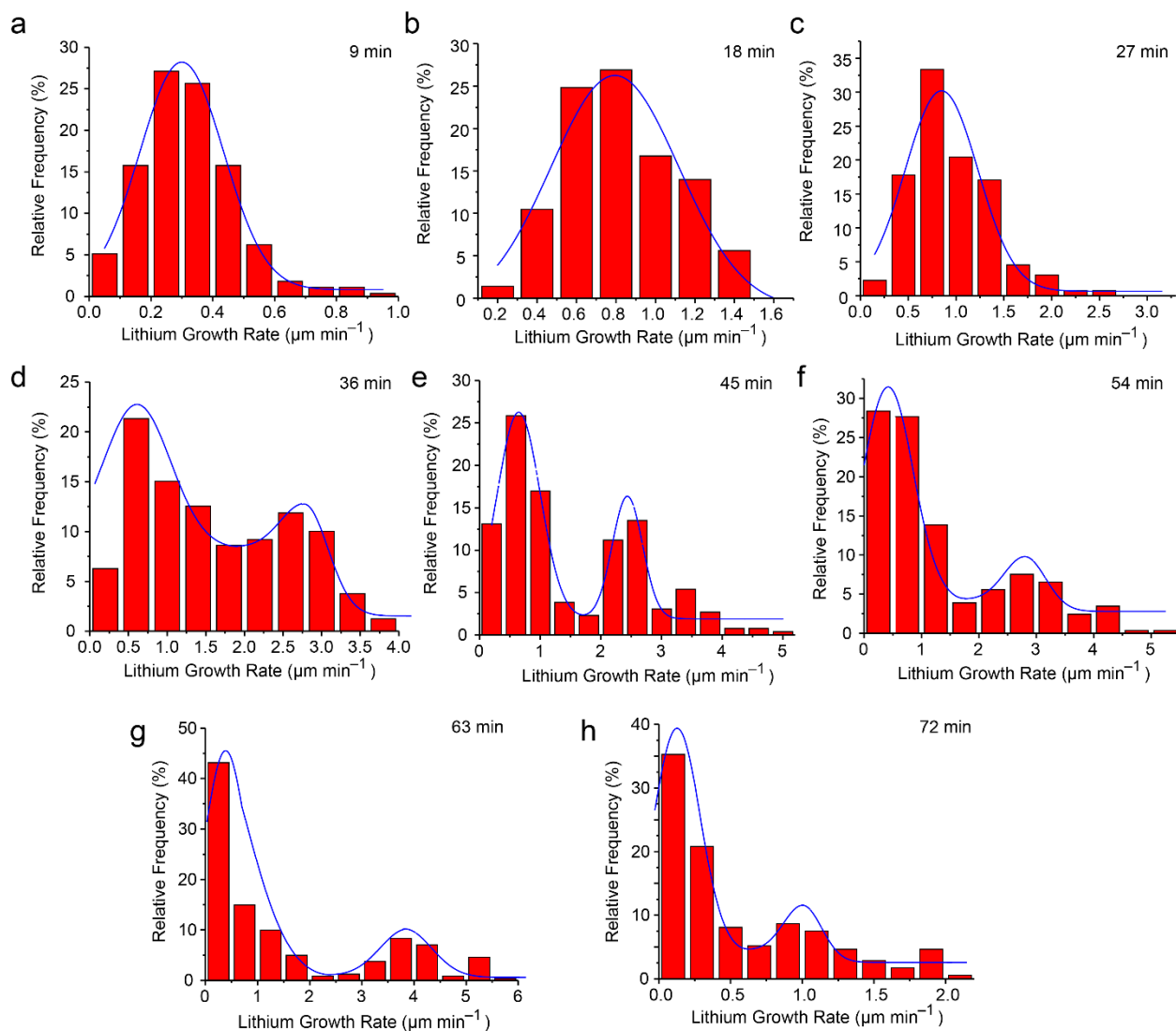
All phase-field simulations were performed by COMSOL Multiphysics 5.2 in a $300 \times 300 \mu m^2$ half-cell. Two scenarios of low (1 mol/L) and high (2 mol/L) electrolyte salt concentrations were simulated for PEO precipitation and no precipitation scenarios, respectively. Major simulation parameters are set to be consistent with the available experimental data. The Li-ion conductivities in electrolyte and PEO precipitate are $10^{-3} S/cm$, $2 \times 10^{-4} S/cm$, respectively. The elastic modulus of Li metal, PEO precipitate and electrolyte are 4.9 GPa, 1.6 GPa, and 10 MPa, respectively. The mechanical interaction between Li metal and electrolyte in the high salt concentration system was considered negligibly small due to the extremely low modulus of the electrolyte phase and the complication of introducing plasticity. Neglecting the impact of the SEI layer, the surface energies of Li metal and PEO used in this simulation are $0.48 J/m^2$ and $0.05 J/m^2$, respectively.^{5,6} Dirichlet boundary conditions were applied for electrolyte bulk concentration. Identical smooth anode surfaces were used as initial morphologies for both simulations (Fig. 3f & 3g). White noise was included in the simulations to mimic thermal fluctuation.



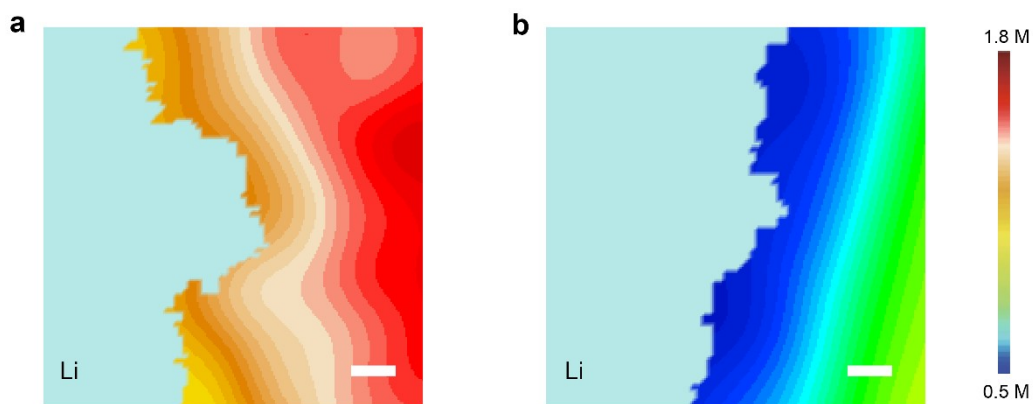
Supplementary Fig. 1. The comparison between spontaneous Raman scattering and stimulated Raman scattering (SRS). Only one laser is used as the excitation laser in spontaneous Raman, and the photons will have an energy loss of Ω after inelastic scattering. In SRS, two different lasers with an energy gap matching Ω will be simultaneously used and result in 10^8 times faster Raman transitions.



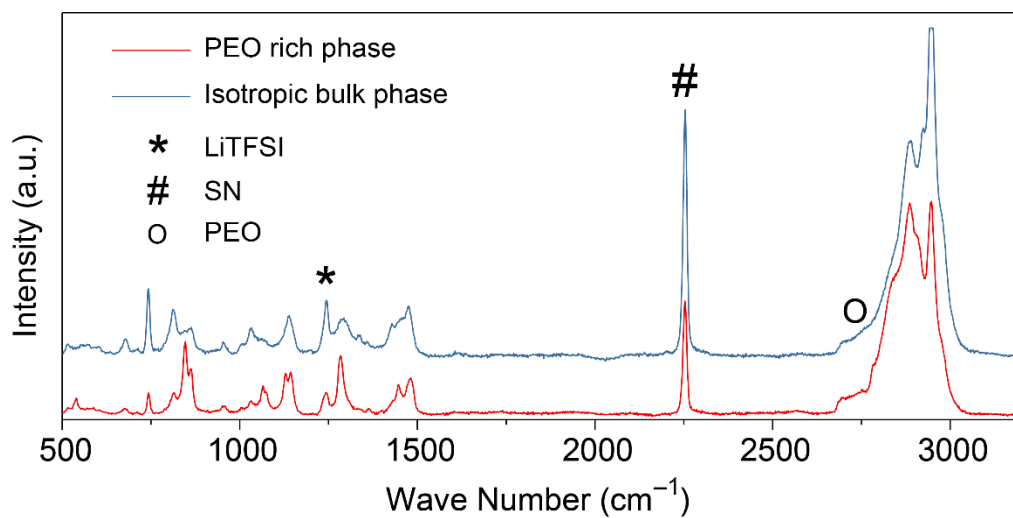
Supplementary Figure 2. Ionic conductivities of HCPE and LCPE at different temperatures. The ionic conductivities of HCPE and LCPE at 21 °C are $1.7 \times 10^{-4} \text{ S cm}^{-1}$ and $1.0 \times 10^{-4} \text{ S cm}^{-1}$, respectively.



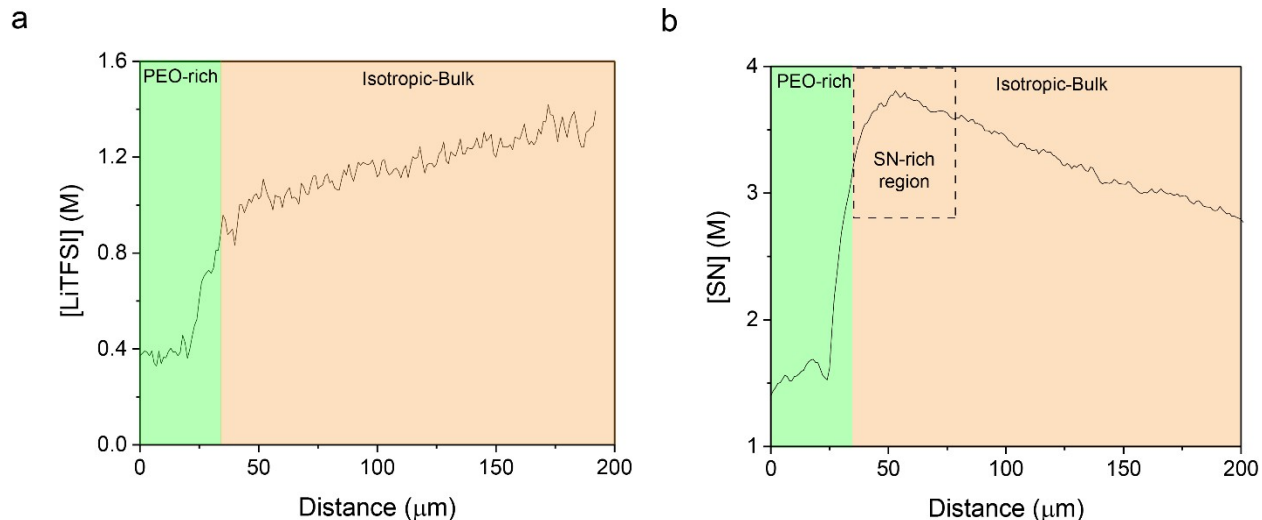
Supplementary Fig. 3. Frequency analysis of the lithium deposition rate in the cell with HCPE. **a-c**, the mossy lithium growth stage ($t = 0$ to 27 min), where the lithium growth pattern fits the normal distribution. **d-h**, the dendrite growth stage ($t = 27$ to 72 min), in which the lithium growth pattern fits dual peak normal distribution, showing that dendrite growth happened on part of the lithium electrode surface.



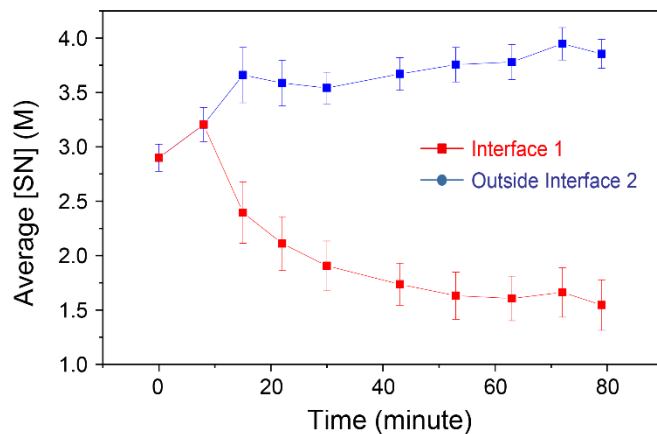
Supplementary Fig. 4. The zoom-in SRS pictures show the fine structures of lithium electrodes and ionic concentration. **a**, the zoom-in picture of **Fig. 2a** at $t = 45$ minutes. **b**, the zoom-in picture of **Fig. 2e** at $t = 30$ minutes. Scale bars are $10 \mu\text{m}$.



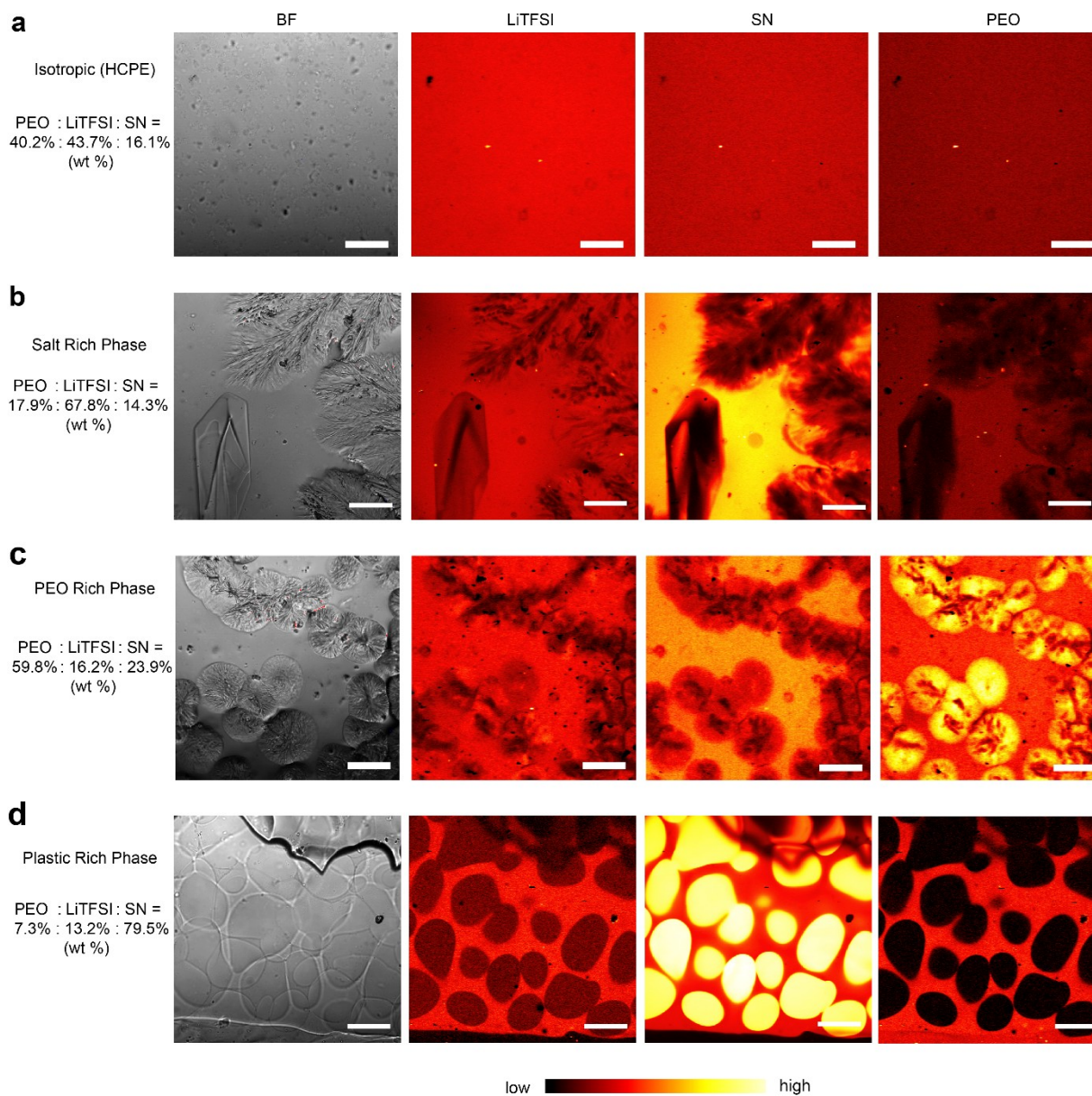
Supplementary Fig. 5. Spontaneous Raman spectra of the new PEO-rich phase formed during lithium deposition and the adjacent isotropic bulk phase. This shows that the new PEO-rich phase contains much less amount of LiTFSI and SN.



Supplementary Fig. 6. Line scans of [LiTFSI] and [SN] along the direction that is perpendicular to the electrode surface show the existence of two phases. **a**, the concentration of LiTFSI and **b**, the concentration of succinonitrile. The data is from the same cell in **Fig. 2e** with LCPE electrolyte. The current density is 0.5 mA cm^{-2} and the deposition time is 79 min. The green and the orange region correspond to the PEO-rich and the isotropic bulk phase, respectively. The PEO-rich phase is poor in both SN and LiTFSI, while the isotropic phase has a much higher [SN] and [LiTFSI]. The excessive SN in the PEO rich phase is repelled into the isotropic bulk polymer electrolyte during phase transformation, leading to an SN-rich region outside the new phase, as marked by the high [SN] in the dashed box in **b**. Hence, the new phase formed at the Li surface is denoted as the PEO-rich phase.

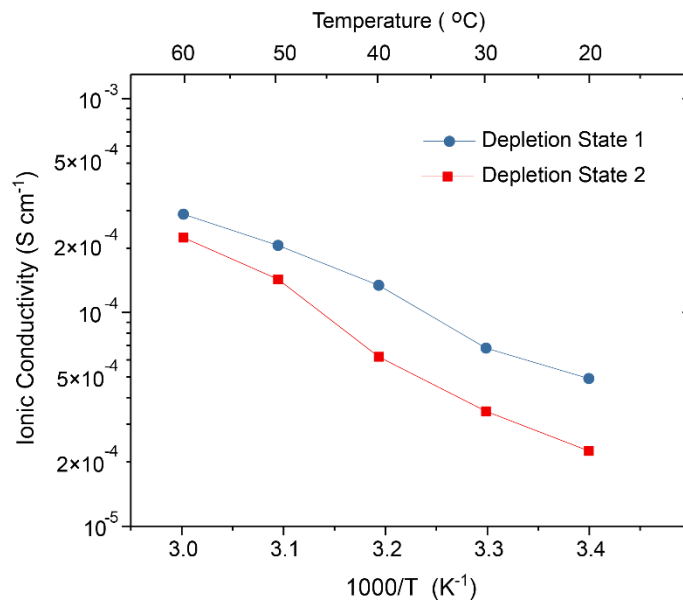


Supplementary Fig. 7. Change of [SN] upon the formation of the new PEO-rich phase. Interface 1 and Interface 2 refer to the boundary between the lithium electrode and the PEO electrolyte, and the boundary between the new PEO-rich phase and the isotropic bulk polymer electrolyte, respectively. The increasing [SN] difference along interface 2 shows that the plasticizer (SN) is progressively repelled from the PEO-rich phase to the bulk electrolyte during the formation of the new PEO-rich phase.

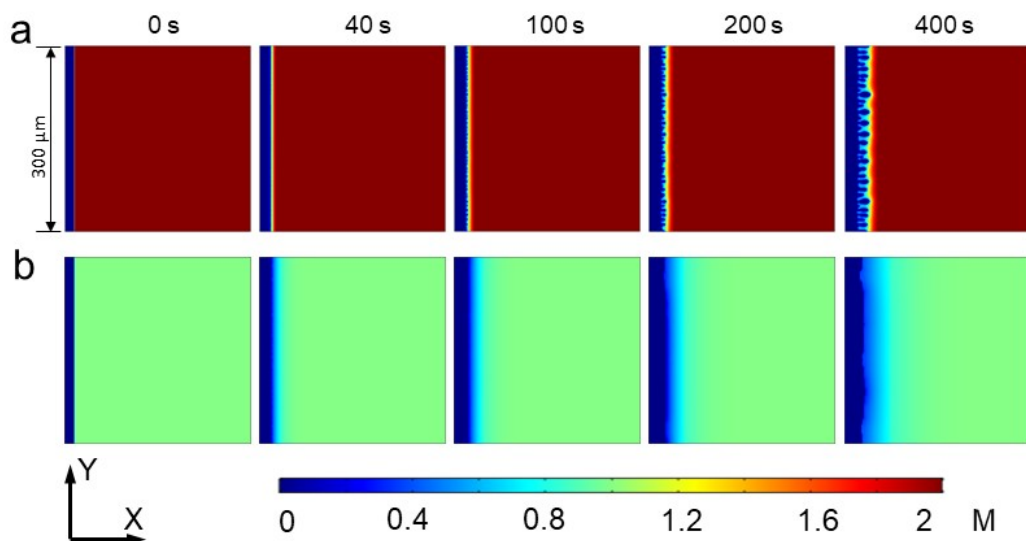


Supplementary Fig. 8. The bright field and SRS pictures of PEO electrolyte with different compositions, including those in the two-phase regions and the single-phase region. Wavenumbers at 1245 cm^{-1} , 2250 cm^{-1} , and 2800 cm^{-1} are selected for SRS imaging of LiTFSI, SN and PEO, respectively. **a**, the isotropic HCPE. **b**, the co-existence of the isotropic phase and the LiTFSI-rich phase. The weight percentage of PEO: LiTFSI:SN is 17.9%: 67.8%: 14.3%. **c**, the co-existence of the isotropic phase and the PEO-rich phase. The weight percentage of PEO: LiTFSI:SN is 59.8%: 16.2%: 23.9%. **d**, the co-existence of the isotropic phase and the SN-rich phase. The weight percentage of PEO: LiTFSI: SN is 7.3%: 13.2%: 79.5%. It worth noting that the bright field image and SRS images do not match in this case. SN-rich phase prefers to form thin sheets at different z-heights and stacks in bright field images. Due to the

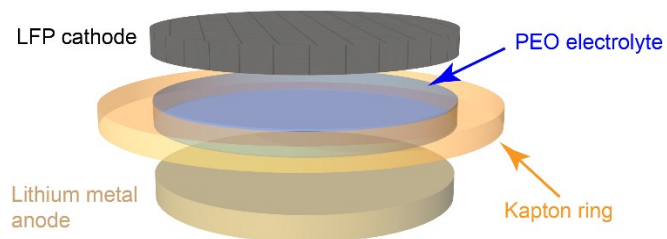
confocal nature of SRS, only one layer is observed in SRS images, which can effectively avoid unnecessary interruptions.



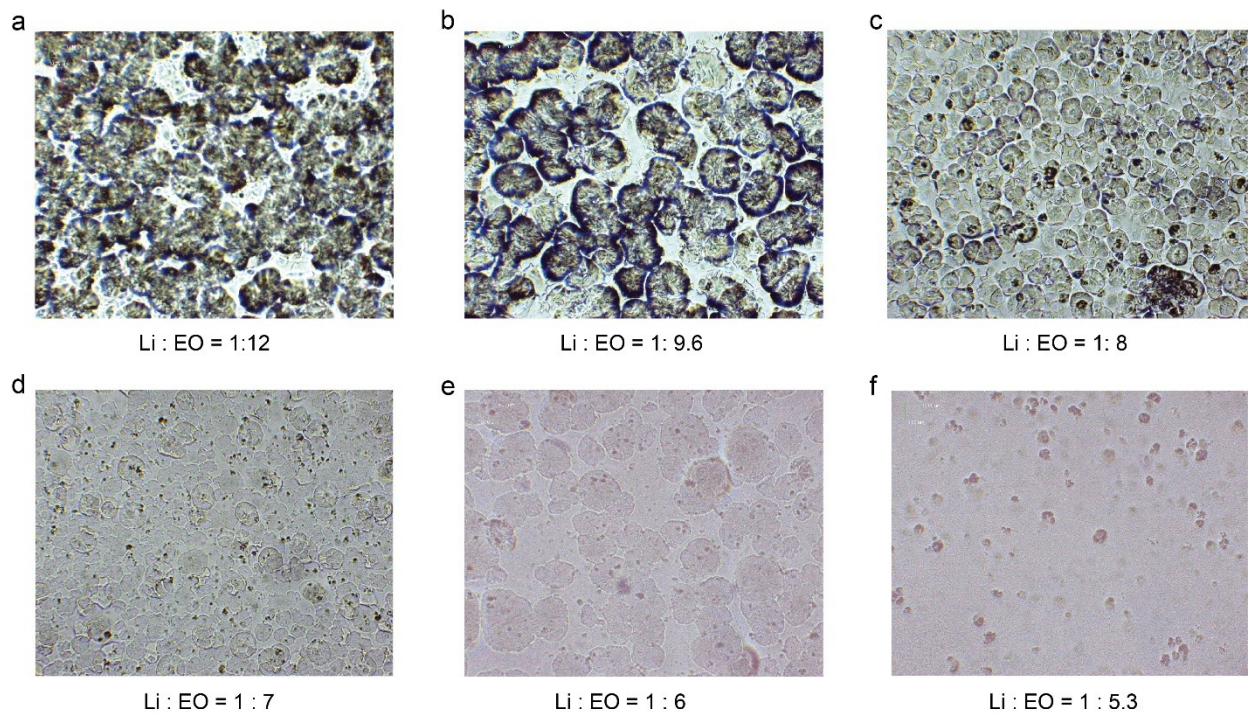
Supplementary Figure 9. Ionic conductivities of PEO-rich phases formed at lithium surface at different temperatures. The compositions of depletion state 1 and 2 are 0.52 M LiTFSI / 2.6 M SN and 0.38 M LiTFSI / 2.3 M SN, respectively, as determined by the SRS microscopy. The ionic conductivities of polymer electrolytes at these two depletion states are $2.3 \times 10^{-5} \text{ S cm}^{-1}$ and $4.9 \times 10^{-5} \text{ S cm}^{-1}$ at 21 °C, respectively.



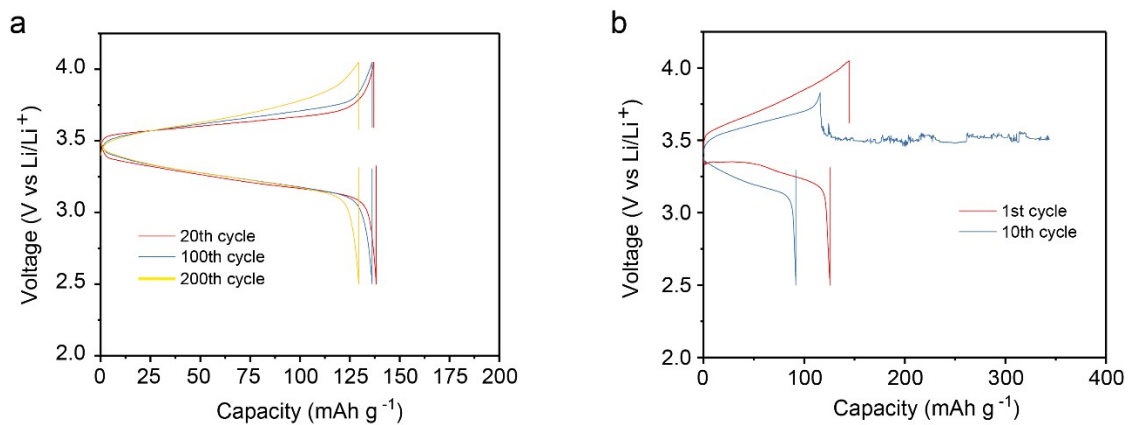
Supplementary Fig. 10. Phase-field simulations of Li electrodeposition in solid polymer electrolytes at different moments show the concentration change in the electrolytes during lithium deposition. The color indicates the concentration of Li salt, where 0 means lithium metal. The simulated current density is 0.5 mA cm^{-2} . The phases of Li metal, PEO precipitate and electrolyte have elastic moduli of 4.9 GPa, 1.6 GPa, and 10 MPa, respectively. The ion conductivities in the bulk electrolyte and the PEO-rich phase are $10^{-3} \text{ S cm}^{-1}$ and $2 \times 10^{-4} \text{ S cm}^{-1}$, respectively. **a**, the electrolyte with 2 M salt, so ions are not depleted even at the final state ($t = 400 \text{ s}$) and **b**, the electrolyte with 1 M salt. Ion depletion induces phase separation which suppresses dendrite growth, which is consistent with experimental observations.



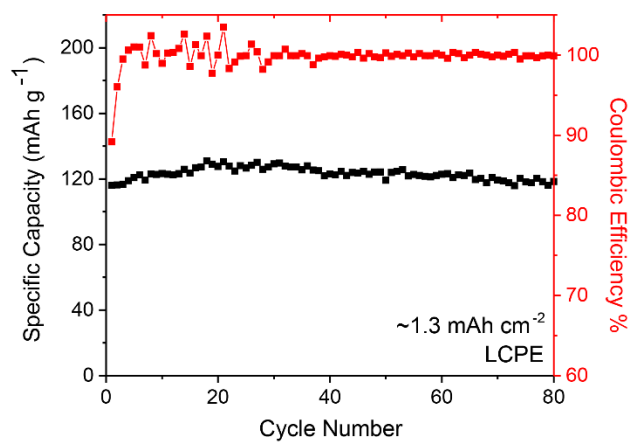
Supplementary Fig. 11. The schematics of an LFP/PEO/Li full cell. A ring made of Kapton tape with a thickness of $\sim 100\ \mu\text{m}$ is used to make sure that the distance between LFP cathode and lithium metal anode is fixed.



Supplementary Fig. 12. The optical images of PEO/LiDFOB+LiBF₄/PC based electrolytes. When the EO : Li is below 6 (f) , the PEO rich phase almost disappears and the electrolyte becomes isotropic.



Supplementary Fig. 13. The voltage profiles of LFP/PEO/Li cells with PC-based (a) LCPE and (b) HCPE. The composition of LCPE is PEO: LiDFOB: LiBF₄ = 12:1:1 (EO/Li⁺ = 6) and the composition of HCPE is EO: LiDFOB: LiBF₄ = 6:1:1 (EO/Li⁺ = 3). In both LCPE and HCPE, propylene carbonate (PC) is used as the plasticizer, whose weight is 90% of PEO.



Supplementary Fig. 14. LFP/PEO/Li cell with cathode mass loading of 10 mg cm⁻², 40 μm thick lithium metal, and PC-based LCPE. The areal capacity of this cell is around 1.3 mAh cm⁻².

Supplementary Table 1. The compositions of overall electrolytes, corresponding PEO-rich and isotropic bulk phases in PEO electrolytes for all points in **Fig. 3e**. The concentration is determined by Raman intensity in SRS images and calibration curves for each material. Wavenumbers at 1245 cm^{-1} and 2250 cm^{-1} are selected for SRS imaging of LiTFSI and SN, respectively.

Overall Concentration		PEO-rich phase		Isotropic bulk phase	
SN (M)	LiTFSI (M)	SN (M)	LiTFSI (M)	SN (M)	LiTFSI (M)
3.8	0	3.8	0	N/A	N/A
3.7	0.23	2.3	0.22	3.2	0.38
3.5	0.44	2.3	0.38	3.9	0.70
3.3	0.63	2.6	0.52	4.6	0.82
3.2	0.80	3.0	0.65	5.7	0.93
3.0	0.99	3.5	0.79	6.6	1.0
2.9	1.1	N/A	N/A	2.9	1.1

Reference

1. Cheng, Q, *et al.* Operando and three-dimensional visualization of anion depletion and lithium growth by stimulated Raman scattering microscopy. *Nat. Commun.* **9**, 2942 (2018).
2. H.-K. Tian, Z. Liu, Y. Ji, L-Q. Chen, Y. Qi, “Interfacial Electronic Properties Dictate Li Dendrite Growth in Solid Electrolytes”, *Chem. Mater.*, **31**, 7351–7359 (2019).
3. L. Chen, H. W. Zhang, L. Y. Liang, Z. Liu, Y. Qi, P. Lu, J. Chen, L. Q. Chen, *J. Power Sources* **300**, 376-385 (2015).
4. H-W. Zhang, Z. Liu, L. Liang, L. Chen, Y. Qi, S. J. Harris, P. Lu, L-Q. Chen, “Understanding and predicting the lithium dendrite formation in Li-ion batteries: Phase field model”, *ECS Transaction*, **61**, 1-9 (2014).
5. Z. Liu, Y. Qi, Y. Lin, L. Chen, P. Lu, L-Q. Chen, “An Interfacial Study of Solid Electrolyte Interphase at Li Metal Anode from Density Functional Theory and its Implication for Li Dendrite Growth”, *J. Electrochem. Soc.*, **163**, A592-A598 (2016).
6. Y. Lin, Z. Liu, L-Q. Chen, Y. Qi, “Connecting the irreversible capacity loss in Li ion batteries with the electronic insulating properties of SEI components”, *J. Power Sources*, **309**, 221-230 (2016).

SI for Stabilizing Lithium Metal Anode by Ion Depletion-ind... (3.52 MiB)

[view on ChemRxiv](#) • [download file](#)

Other files

Suppl Movie 6.mp4 (4.44 MiB)

[view on ChemRxiv](#) • [download file](#)

Suppl Movie 5.mp4 (10.76 MiB)

[view on ChemRxiv](#) • [download file](#)

Suppl Movie 4.mp4 (1.72 MiB)

[view on ChemRxiv](#) • [download file](#)

Suppl Movie 3.mp4 (2.51 MiB)

[view on ChemRxiv](#) • [download file](#)

Suppl Movie 2.mp4 (2.57 MiB)

[view on ChemRxiv](#) • [download file](#)

Suppl Movie 1.mp4 (1.09 MiB)

[view on ChemRxiv](#) • [download file](#)
